This is the Pre-Published Version.

https://doi.org/10.1016/j.compstruct.2022.116513

Accepted by ***Composite Structures (Elsevier)***, Nov. 2022

Shear Strengthening of Reinforced Concrete Beams Using Geopolymer-Bonded Small-Diameter FRP Bars

Kai-Di Peng [1]; Jun-Qi Huang [2]; Bo-Tao Huang [3] (*); Ling-Yu Xu [4]; Jian-Guo Dai [5] (*)

Highlights

- Shear performance of FRGM-strengthened RC beams was explored for the first time.
- Geopolymer- and epoxy-bonded FRGM had similar shear strengthening efficiencies.
- Adding steel fibers into FRGM improved the shear capacity of strengthened RC beams.
- An analytical model was proposed to predict the shear capacity of FRGM-strengthened beams.

Abstract

In this study, a comprehensive investigation on the shear behavior of RC beams strengthened with small-diameter CFRP bar-reinforced geopolymer matrix (FRGM) system is presented for the first time. A total of twelve RC beams, including two reference beams and ten strengthened beams, were prepared and tested. Five factors were considered, including bonding methods (geopolymer-bonded *vs.* epoxy-bonded), matrix types (slag-to-fly ash ratios of 9:1 *vs.* 6:4), alignment directions of small-diameter CFRP bars (90° *vs.* 45° to the longitudinal direction), configurations of FRGM layers (single-side *vs.* double-side), and shear span-to-depth ratios of RC beams (a/d = 2.4 *vs.* 3.2). The strengthening efficiency of RC beams with the double-side FRGM layer (1.9 times that of the reference beam) was found to be much larger than that of the RC beams with the single-side FRGM layer (1.2 times that of the reference beam). In addition, the geopolymer-bonded layer showed a similar load capacity (approximately 98%) with its epoxy-bonded counterpart. The use of steel fibers in geopolymer matrix further restrained the development of shear cracks and improved the shear capacity. Finally, a theoretical analysis method was proposed for predicting the shear capacity of the FRGM-strengthened RC beams.

Keywords

Fiber-Reinforced Polymer (FRP); Small-diameter FRP bar; Geopolymer; Alkali-activated fly ash/slag; Shear strengthening; Reinforced concrete

---

[1] Engineer, Real Estate Group Co., Ltd., China Construction Communication Group (CCCG), Beijing, China; Ph.D., Department of Civil and Environmental Engineering, The Hong Kong Polytechnic University, Hong Kong, China. E-mail: kaidi01.peng@connect.polyu.hk

[2] Assistant Professor, School of Civil and Hydraulic Engineering, Hefei University of Technology, Hefei, Anhui, China. E-mail: 2019800122@hfut.edu.cn

[3] ZJU100 Young Professor, Institute of Advanced Engineering Structures, Zhejiang University, Hangzhou, China; Research Fellow, Department of Civil and Environmental Engineering, The Hong Kong Polytechnic University, Hong Kong, China. E-mail: botaohuang@zju.edu.cn (**Corresponding Author*)

[4] Ph.D. Candidate, Department of Civil and Environmental Engineering, The Hong Kong Polytechnic University, Hong Kong, China. E-mail: ling-yu.xu@connect.polyu.hk

[5] Professor, Department of Civil and Environmental Engineering, The Hong Kong Polytechnic University, Hong Kong, China. E-mail: cejgdai@polyu.edu.hk (**Corresponding Author*)

1 Introduction

Concrete is the most widely used man-made engineering material, which is commonly made by cementitious binders, aggregates, and water [1]. Also, reinforced concrete (RC) structures are widely used in civil engineering structures [2, 3, 4, 5] and protection structures [6, 7]. The strengthening of RC members is an essential topic for structural engineering researchers and practitioners [8, 9, 10, 11]. An RC beam may fail under either flexural or shear loads, and numerous research efforts have been made on flexural (e.g., [12, 13, 14, 15, 16]) and shear (e.g., [17, 18, 19, 20]) strengthening of RC beams. Normally, the shear failure occurs suddenly without sufficient pre-warning (i.e., a brittle failure) [17, 18, 21, 22]. Therefore, for safety concerns, the shear strength of RC members should be designed significantly larger than their flexural strength to achieve a ductile failure at the ultimate state.

Fiber-reinforced polymer (FRP) composites have been widely used in concrete structural members [23, 24, 25, 26, 27, 28, 29, 30], and epoxy resin is commonly used as the bonding adhesive in the FRP strengthening systems. In recent decades, several shear strengthening methods using FRP composites have been proposed, including externally-bonded FRP sheet/plate and near-surface mounted FRP strip/rod to the surface of RC beams [9, 17, 18, 21, 31, 32]. Particularly, FRP could be applied to strengthen structures with enhanced resistance to blast loading [31, 32]. Also, the use of FRP composites in shear strengthening of RC beams has been proved very effective, and the maximum improvement of the shear capacity could be two times that of the un-strengthened counterpart [9, 33]. However, the relatively poor resistance of the epoxy-bonded FRP strengthening system to fire has been noticed [34, 35, 36]. When FRP composites are exposed to fire (typically above 300°C), they will undergo thermal decomposition. The results of existing studies have clearly shown a significant problem of epoxy-bonded FRP in high temperature/fire environments [37, 38, 39]. In addition, some other concerns for the epoxy-bonded FRP system arise from its poor resistance under ultraviolet radiation [40] and the lower epoxy/concrete compatibility under temperature variation and moisture attack [39, 41, 42, 43].

To overcome the above-mentioned drawbacks of epoxy-bonded FRP strengthening systems, fabric-reinforced cementitious matrix (FRCM) systems [44, 45, 46], often in the form of textile-reinforced mortar (TRM) [47, 48, 49] or textile-reinforced concrete (TRC) systems [50], have been proposed as an emerging alternative for the strengthening of RC members. The FRCM strengthening systems are commonly composed of fabric/textile reinforcement and inorganic cement-based matrix [46]. The available reinforcement used in the FRCM strengthening system can be classified as un-impregnated fibers [45, 48, 49], including dry fiber sheet and fiber textile/mesh, and resin-impregnated fibers (e.g., FRP grids and FRP bars) [13, 20, 51]. It should be noted that the average fracture strain of fabric/textile in the FRCM layer is usually significantly lower than that achieved in the epoxy-bonded FRP strengthening system due to the inefficient fiber/matrix stress transfer of the former method [13]. Therefore, the FRP bar/grid, in which fibers have been impregnated with epoxy resin, is an optimal choice to improve the stress efficiency of FRP reinforcement [20, 51]. For the FRP grid, the fiber content is comparatively less than that of FRP bars, and the material efficiency of FRP grids is lower as the fibers are arranged in two perpendicular directions [51]. For the normal-size FRP bars in the strengthening layer, an effective anchorage of the strengthening system to the RC members is still essential to guarantee the bond strength [51].

In the FRCM strengthening system, the inorganic matrix plays an important role as it acts as a medium for transferring stress from the concrete substrate to the reinforcement [52, 53, 54]. In particular, the low tensile strength of the inorganic matrix generally leads to localized cracks which affect the interfacial stress transfer between concrete substrate and reinforcement in FRCM [13, 55]. Therefore, adding short fibers in the in-organic matrix has been explored and found to improve the tension stiffening effect and enhance the strengthening efficiency of the FRCM strengthening system [13,20]. Particularly, strain-hardening cementitious composites are ideal matrix materials for the FRCM system, whose tensile strain-hardening behavior can be achieved through the proper use of steel fibers, polyvinyl alcohol (PVA) fibers and polyethylene (PE) fibers [56, 57, 58, 59, 60, 61, 62]. According to the existing studies, the in-organic matrices can be made from different types of mortars, such as Portland cement mortar, polymer-modified mortar, geopolymer mortar and magnesium oxychloride/phosphate cement mortar [63, 64, 65, 66, 67]. To improve the sustainability of cement-based matrix, geopolymer matrix is a greener alternative to Portland cement [68, 69, 70, 71, 72, 73], as aluminosilicate industrial by-products/wastes and sodium/potassium-based activators are commonly utilized as raw materials. From the current technology, short fiber reinforcement can be used to enhance the toughness of geopolymer matrix [74, 75, 76], and geopolymer concrete members can also be reinforced by FRP bars [77, 78].

Very recently, the authors introduced a geopolymer-bonded small-diameter FRP system to strengthen RC structures [79]. In this system, geopolymer exhibits a superior bond with concrete [80, 81] and better fire resistance than ordinary cementitious matrix and organic adhesives [82, 83]. In addition, smaller-diameter FRP bars (with a diameter of 3 to 10 mm) have larger specific surface area, which results in a better bond interaction between the bar and the concrete/geopolymer matrix [84, 85, 86]. It is noted that the diameter of FRP bars commonly ranges from few millimeters to a few tens of millimeters. As the strengthening of RC members based on small-diameter FRP-reinforced geopolymer matrix (FRGM) is an emerging method, the existing studies have only explored the flexural strengthening [79] and the bond performance between small-diameter FRP bars and geopolymer [86]. However, in order to avoid a brittle failure, the shear strength of RC members needs to be significantly larger than their flexural strength. Therefore, it is necessary to ascertain the efficiency of the shear strengthening of this new FRGM system for future applications. Up to now, there is no literature on the shear strengthening performance of this emerging system. In addition, the existing knowledge on the shear design of the FRGM-strengthened RC member is also quite limited.

In this study, a comprehensive experimental investigation was carried out to evaluate the shear performance of FRGM-strengthened RC beams. The influences of various design parameters on the shear strengthening effect were explored and discussed, which can facilitate valuable knowledge for the design and application of the FRGM system with small-diameter FRP bars.

2 Experimental programs

2.1 Materials

The geopolymer matrix was produced using industrial by-products (i.e., fly ash and slag), river sand, and alkaline activators. The mix proportions of three different types of geopolymers are listed in **Table 1**. The alkaline activator was comprised of liquid sodium silicate and sodium carbonate (Na_2CO_3) pellets. The liquid sodium silicate (waterglass) had a solid content of 35% and a SiO_2/Na_2O molar ratio of 3.3. The sodium carbonate had a purity of 99%. According to the author’s previous work [80], the increase in the slag-to-fly ash ratio of geopolymer could improve its bond strength with the concrete substrate. Thus, the two mixes of plain geopolymer mortars (i.e., M-H and M-N in **Table 1**) were prepared with different slag-to-fly ash ratios (i.e., 9:1 and 6:4). Fiber-reinforced geopolymer (M-S in **Table 1**) was also prepared using the matrix of M-H and 2.0% (Vol.) steel fibers. It should be noted that the amount of water used in geopolymer M-H, M-N, and M-S was slightly adjusted to achieve similar workability.

Table 1 Mix proportions of geopolymer (weight ratio)

Raw materials	M-H	M-N	M-S
Fly ash	0.100	0.400	0.100
Slag	0.900	0.600	0.900
River Sand	1.500	1.500	1.500
Sodium Carbonate	0.076	0.076	0.076
Waterglass	0.120	0.120	0.120
Water	0.250	0.240	0.250
Steel fiber	/	/	2.0% (Vol.)

The compressive strength of geopolymer mortar was determined using the cube specimens with a side length of 50 mm following ASTM C109/C109 M [87]. The compressive strengths of geopolymer M-H, M-N, and M-S at 28 d were 106.3 MPa, 89.6 MPa, and 111.5 MPa, respectively.

Ready-mixed normal-strength concrete was provided by a local supplier, Guangzhou Hengtai concrete mixing plant. The compressive performance of the concrete was determined by three standard cylinders (Φ150 mm × 300 mm) following ASTM C39 / C39M [88]. The compressive strength and peak strain of concrete were 59.6 MPa and 0.23%, respectively.

Sand-coated small-diameter carbon FRP (CFRP) bars with a diameter of 3 mm (**Fig. 1a**) were employed as the internal reinforcement of the FRGM strengthening system. To fix CFRP bars in the strengthening layer, two glass FRP (GFRP) bars with a diameter of 6 mm were used (**Fig. 2**). According to ASTM D7205 / D7205M [89], five samples of each type of FRP bars were tested to measure their mechanical properties. The results are summarized in **Table 2**, including the tensile strength, tensile strain capacity, and elastic modulus. The properties of steel bars are also summarized in **Table 2**. Three samples of each type of steel bars were also tested, following the instructions of ASTM A370 [90].

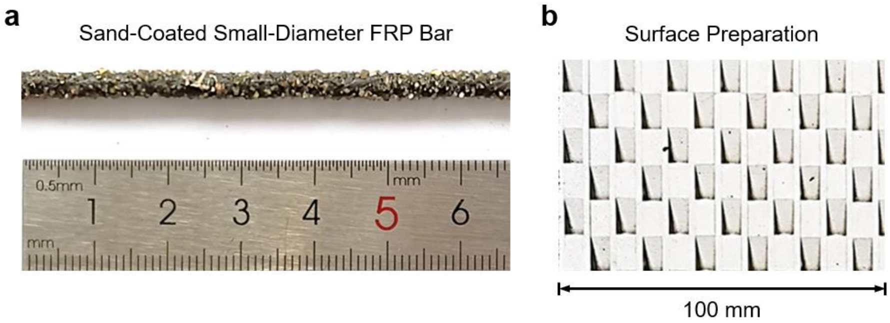

Fig. 1 (a) Small-diameter CFRP bar and (b) concrete surface preparation.

Table 2 Mechanical properties of reinforcements.

Materials	Diameter (mm)	Tensile Strength (MPa)	Yield Strength (MPa)	Strain at the end of yield plateau (%)	Tensile Strain Capacity (%)	Elastic Modulus (GPa)
CFRP_D03	3	2455	/	/	1.6	154
GFRP_D06	6	1216	/	/	2.3	53
Steel bar_D10	10	483	251	/	19.0	200
Steel bar_D14	14	687	469	1.9	19.0	200
Steel bar_D25	25	622	416	1.6	20.5	200

2.2 Beam specimens and testing methods

A total of twelve shear-critical RC beams were prepared. The details of RC beams are shown in **Fig. 2**. 25-mm-diameter and 14-mm-diameter steel bars were used as the longitudinal reinforcements in the tension and compression zones, respectively. All the RC beams had a rectangular cross-section (150 mm × 300 mm), and the effective depth was 270 mm. Commonly, RC beam specimens can be divided into three different types, deep beams ($a/d < 1.0$), short beams ($1.0 < a/d < 2.5$), and ordinary shallow beams ($a/d > 2.5$), where the "a" and "d" represented the shear span length and effective depth of RC beam [20], respectively. Here, two different types of RC beams, short beams ($a/d = 2.4$) and ordinary shallow beams ($a/d = 3.2$) were prepared with the shear spans of 650 mm and 850 mm. For the specimens in **Fig. 2**, one shear span was heavily reinforced with stirrups while the other shear span had no stirrups. The shear strengthening was carried out on the side without stirrups and the shear failure was also designed to occur at this side. Surface treatment of the strengthening area in the concrete beam was facilitated by the grooves with a triangle section (length: 11 mm, width: 6 mm, and the maximum depth: 7 mm), as shown in **Fig. 1b**.

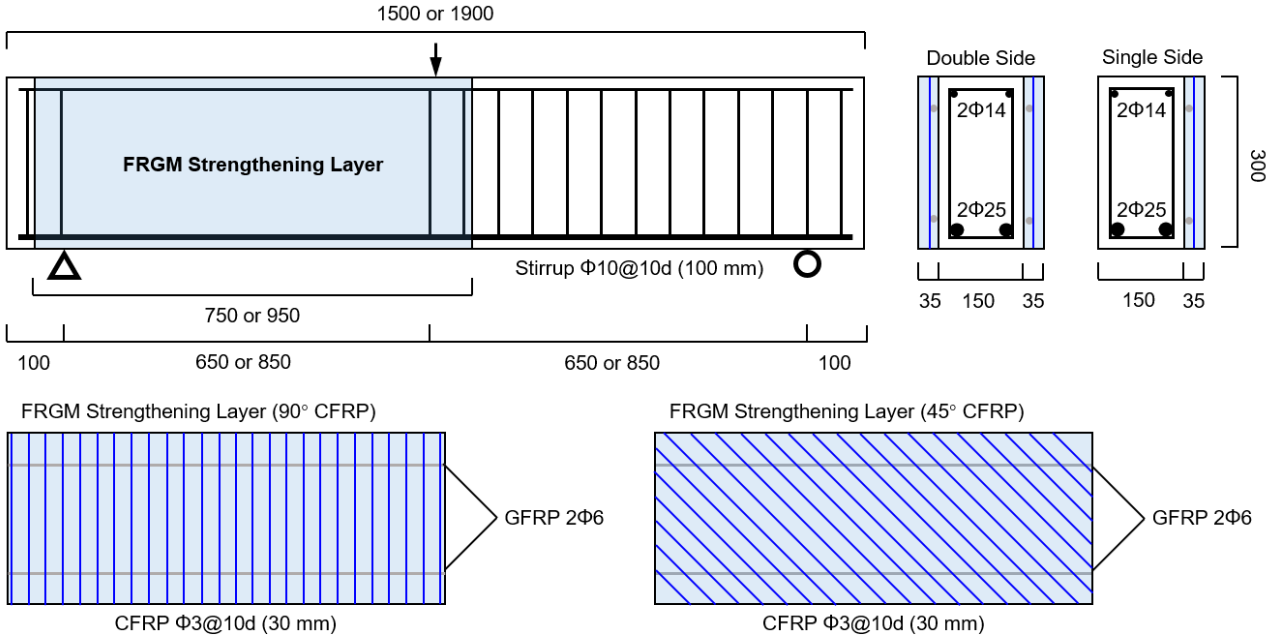

Fig. 2 Specimen dimensions.

The details of the FRGM layer are shown in **Fig. 2**, where the thickness and height are 35 mm and 300 mm, respectively. The length of the FRGM layer was 750 mm or 950 mm. In the FRGM layer, 3-mm small-diameter CFRP bars with a spacing of 30 mm (10d) were used as the shear reinforcement, and two 6-mm GFRP bars were used to fix the small-diameter CFRP bars.

The specimen details of the RC beams are listed in **Table 3**. The factors considered in this study include the shear span-to-depth ratio of RC beams (2.4 *vs.* 3.2), the configuration of the strengthening layers (single-side *vs.* double-side), bonding methods (geopolymer-bonded *vs.* epoxy-bonded), slag-to-fly ash ratios in geopolymer matrix (i.e., 9:1 *vs.* 6:4), short fiber reinforcement conditions in the matrix (plain geopolymer *vs.* steel fiber-reinforced geopolymer), and the alignment directions of small-diameter CFRP bars [90° (vertical) *vs.* 45° to the longitudinal direction]. It is noted that according to existing literature [17, 91], the orientation of FRP bars/sheets (as shear reinforcement) would affect the shear behavior of strengthened RC beams. Compared with FRP bars placed at 90° direction, the bars placed at 45° direction could contribute more to shear resistance, because the bar orientation would be perpendicular to the diagonal crack. Considering this, two alignment directions of mini CFRP bars were investigated in this study.

All beam specimens were strengthened with the FRGM layer through in-situ construction except one for which the epoxy resin was used for bonding the prefabricated FRGM layer to make comparisons (see AS-I-E in **Table 3**). The bond strength, tensile strength, and shear strength of the resin were 7 MPa, 50 MPa, and 30 MPa, respectively (provided by the manufacturer). In the specimen IDs, "A" and "B" present the RC beams with two different shear span-to-depth ratios; "0" stands for the reference beam; "H", "N", and "S" stand for three types of geopolymer mortars in **Table 1**; "I" and "II" mean the number of FRGM strengthening layer applied on the RC beams, representing single-side and double-side strengthening, respectively; "E" stand for epoxy-bonded condition; and "45" stands for the small-diameter CFRP bars with an angle of 45° to the longitudinal direction.

Table 3 Specimen details.

Specimen ID	Shear Span-to-Depth Ratio	Reinforcement Ratio (%)	Geopolymer Matrix	No. of FRGM Layer	Angle (°)	Bonding Method
A0	2.4	2.87	/	/	/	/
AN-I	2.4	2.87	M-N	1	90	Geopolymer Bonding
AH-I	2.4	2.87	M-H	1	90	Geopolymer Bonding
AN-II	2.4	2.87	M-N	2	90	Geopolymer Bonding
AH-II	2.4	2.87	M-H	2	90	Geopolymer Bonding
AH-I-45	2.4	2.87	M-H	1	45	Geopolymer Bonding
AS-I	2.4	2.87	M-S	1	90	Geopolymer Bonding
AS-I-E	2.4	2.87	M-S	1	90	Epoxy Bonding
B0	3.2	2.87	/	/	/	/
BN-I	3.2	2.87	M-N	1	90	Geopolymer Bonding
BH-I	3.2	2.87	M-H	1	90	Geopolymer Bonding
BS-I	3.2	2.87	M-S	1	90	Geopolymer Bonding

Note: "No. of FRGM layer" means the number of FRGM strengthening layers (single-side or double-side); "Angle" means the angle of small-diameter CFRP bars aligned to the beam's longitudinal axis; "Geopolymer Bonding" means that the FRGM layer was cast in place; and "Epoxy Bonding" means that the FRGM layer was prefabricated and then bonded to the RC beams using epoxy.

2.3 Experimental programs

Fig. 3 presents the experimental flowchart of the beam specimens in **Table 3**. The control beams (i.e., A0 and B0) were tested at the age of 56 days (28 days + 28 days in **Fig. 3**). For the single FRGM layer-strengthened specimens, the RC beams were cured for 28 days and then the FRGM layer was applied. For the double layer-strengthened ones, the interval between the casting time of two FRGM layers was 3-day. After another 28-day curing, the specimens with single and double FRGM layers were tested. For Beam AS-I-E, the epoxy-bonded prefabricated FRGM layer (cured for 28 days) was used as the strengthening layer, and the specimen was cured for 7 days after the epoxy bonding.

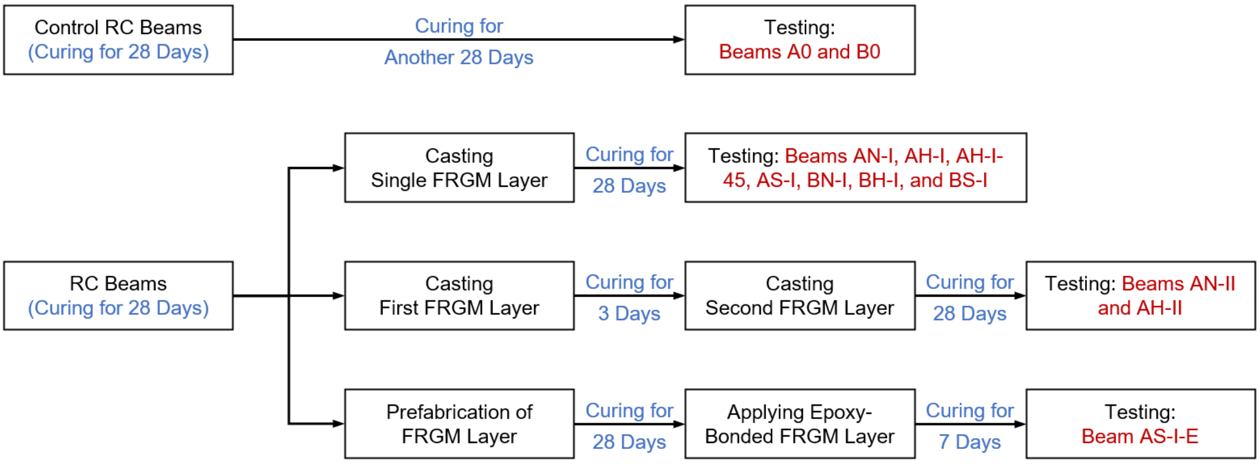

Fig. 3 Experimental flowchart of beam specimens.

The three-point bending test was conducted to investigate the shear performance of the strengthened and reference beams (**Fig. 4**). The vertical displacements at the two supports and the mid-span of the beams were measured using linear variable differential transformers (LVDTs). All the test data were recorded simultaneously by a datalogger at a frequency of 1 Hz. In addition, the DIC technique was used to monitor the strain field and cracking behavior of the beam specimens [92, 93, 94].

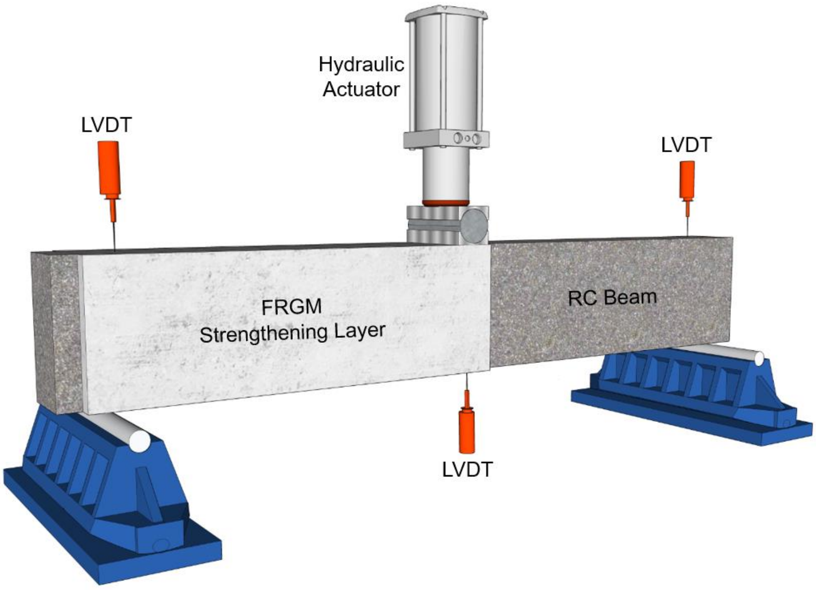

Fig. 4 Schematic diagram of the set-up of the three-point bending test.

3 Shear performance of FRGM-strengthened RC beams

3.1 Load-deflection responses

Fig. 5 presents the load *vs.* mid-span deflection relations of the FRGM-strengthened RC beams and the reference beams (i.e., A0 and B0). **Fig. 6** summarizes the peak loads of all the beams. In **Fig. 5**, the specimens are divided into three groups for comparison. Here, **Fig. 5a** compares the performances of specimens with different numbers of FRGM layers (single-side and double-side) and the slag contents in the geopolymer matrix; **Fig. 5b** compares the performances of specimens with varying fiber contents, the bonding methods, and directions of small-diameter FRP bars in the FRGM layer; and **Fig. 5c** shows the performances of specimens with a shear span-to-depth ratio of 3.2.

Generally, the curves of the specimens in **Fig. 5** could be divided into four parts, which were “before crack load”, “crack load – diagonal crack load”, “diagonal crack load – peak load”, and “peak load – failure”. At the first stage (i.e., before crack load), the load increased almost linearly with the deflection, when the loads of approximately 60 kN and 50 kN were reached for specimens of A and B series, respectively. Afterwards (i.e., crack load – diagonal crack load), the slopes of the curves declined and the curves presented a non-linear increase. When the diagonal crack emerged (i.e., diagonal crack load – peak load), the slopes of the curves presented a second degradation, while a non-linear increase was still seen until the peak load. At the final stage (peak load – failure), a sudden drop could be observed, indicating the shear failure of the specimens. It should be pointed out that for specimen AH-II in **Fig. 5a** and BS-I in **Fig. 5c**, critical shear cracks were observed after the peak loads, but the load-deflection curves still showed a platform stage. Because of this unexpected phenomenon and the limitation of the testing system, the test stopped at the mid-span deflection of 12.5 mm, and the decreasing parts of the load-deflection curves were not measured. The crack patterns and failure processes of these two specimens will still be presented in the following sections.

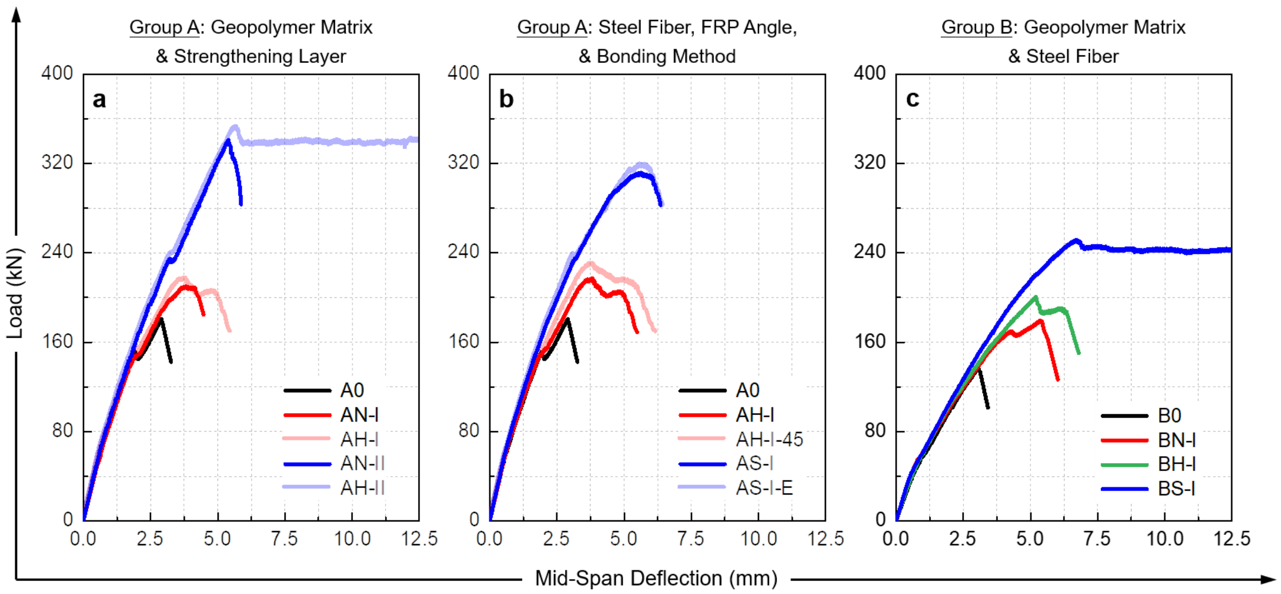

Fig. 5 Load-deflection curves of FRGM-strengthened concrete beams.

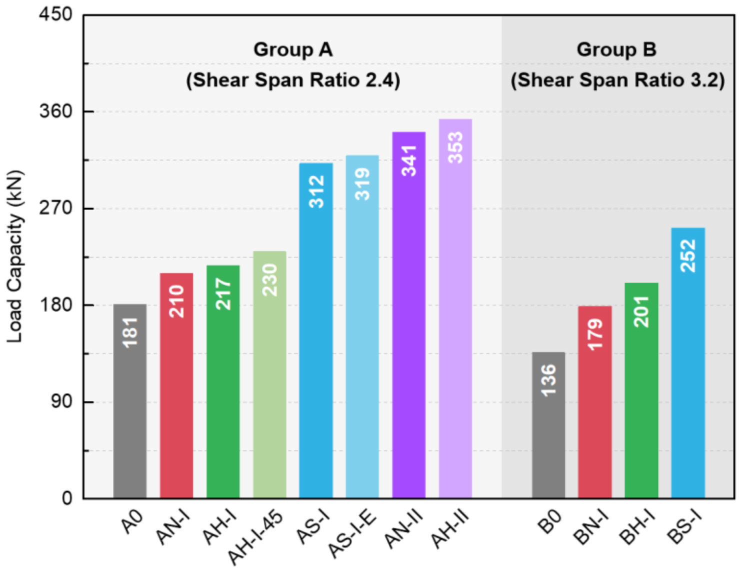

Fig. 6 Ultimate loads of FRGM-strengthened concrete beams.

Comparing the curves in **Fig. 5a** and the corresponding values in **Fig. 6**, it can be found that all the specimens in **Fig. 5a** had almost the similar stiffness in the first and second stages (i.e., from the initial stage to the diagonal crack load), indicating that the FRGM layer provided a marginal influence on the initial and post-crack stiffness of the specimens, which was possibly due to the dominant flexural deformation before the initiation of the diagonal shear crack. With the increase of the number of FRGM layers (i.e., from single layer to double layers), the peak loads of the specimens showed a significant increase. Here, the peak load of the specimen with a single FRGM layer was approximately 1.2 times that of the reference beam, while the peak load of the specimen with double FRGM layers was approximately 1.9 times that of the reference beam. In addition, the slag-to-fly ash ratio of the geopolymer matrix (i.e., 1:9 for Beam AH-II and 4:6 for Beam AN-II) presented a marginal effect on the peak load of the specimens.

For the results in **Fig. 5b** and the corresponding values in **Fig. 6**, it can be found that the peak load of Beam AH-I was higher than that of the specimen strengthened by 45° small-diameter FRP bars (i.e., AH-I-45), indicating that the direction of the small-diameter FRP bars in the FRGM layer affected the peak load of the strengthened beams. The load contribution of the strengthening layer in Beam AH-I was 36 kN, while that in Beam AH-I-45 was 49 kN. It indicated that the shear contribution of 45° FRP bars was 36% higher than that of 90° FRP bars. The peak load of Beam AS-I was 1.4 times that of Beam AH-I, indicating that the addition of steel fibers in the geopolymer matrix significantly improved the peak load of the strengthened beams. On the other hand, the geopolymer- and epoxy-bonded FRGM layers showed the similar strengthening efficiency. The peak loads of Beam AS-I (geopolymer-bonded) and Beam AS-I-E (epoxy-bonded) were 312 kN and 319 kN, respectively.

Fig. 5c shows the load-deflection curves of the specimens with a shear span-to-depth ratio of 3.2, and the results from the experimental investigations seemed to be similar to those discussed in the above section. The slag-to-fly ash ratios of the geopolymer matrix in BH-I and BN-I were 1:9 and 4:6, respectively. At the same time, the obtained peak load of Beam BH-I was slightly higher than that of Beam BN-I (i.e., 1.12 times that of Beam BN-I). Furthermore, by adding 2% (Vol.) steel fibers in the geopolymer matrix, the peak load of the Beam BS-I was 1.25 times that of the specimen without steel fiber in the geopolymer matrix (i.e., Beam BH-I). Compared with the curves in **Fig. 5a** and **Fig. 5b** (shear span-to-depth ratio of 2.4), the curves in **Fig. 5c** (shear span-to-depth ratio of 3.2) showed lower peak loads as expected. For the specimens with the shear span-to-depth ratio of 2.4, the load seemed to present a sudden drop when the diagonal crack initiated. After that, a non-linear load increase with the reduced curve slope could be observed. However, for the specimens with the shear span-to-depth ratio of 3.2, the curve reflected a relatively smooth transmission when the diagonal crack occurred.

3.2 Crack patterns and failure modes

The crack patterns of the FRGM-strengthened beams and the reference beam are shown in **Fig. 7**, and the governing cracks at the ultimate state are marked with thick lines.

The group A specimens showed three types of failure modes. First, a governing diagonal crack developing from the support to the loading point could be seen for the reference RC beam A0 and the strengthened beam AN-I, AH-I, AN-II, and AH-I-45. In addition, concrete crushing could be observed near the loading point, which reflected a typical shear-compression failure. Apart from the governing diagonal crack, additional diagonal or vertical cracks could also be observed in the shear span region. However, for the Beam AH-II, owing to the use of a double-layer higher-strength geopolymer matrix

(M-H), the critical diagonal crack did not propagate throughout the whole section of the beam. For the specimens using fiber-reinforced geopolymer matrix (i.e., Beam AS-I and AS-I-E), the slope of the critical diagonal crack seemed to be larger than that of the specimen using a plain geopolymer matrix Because the existence of steel fibers restrained the opening of the shear crack. Several cracks also existed near the critical shear crack, and the epoxy-bonded specimens (i.e., AS-I-E) had more diagonal cracks than the geopolymer-bonded specimens (i.e., AS-I). It should be pointed out that the critical shear cracks of the RC layer of Beam AS-I will be further analyzed in ***Section 4.2*** to understand the failure process of the beam with steel fiber-reinforced geopolymer.

The group B specimens showed two types of failure modes. For the reference beam B0 and the strengthened beams BN-I and BH-I, the diagonal cracks propagated almost horizontally near the support (at the height of the longitudinal steel rebar). No concrete crushing could be observed at the end of the loading stage, and these specimens were governed by the diagonal tension failure. For the specimen using the fiber-reinforced geopolymer matrix (i.e., BS-I), the slope of the critical crack was also larger than that of the specimens using the plain geopolymer matrix (i.e., BH-I).

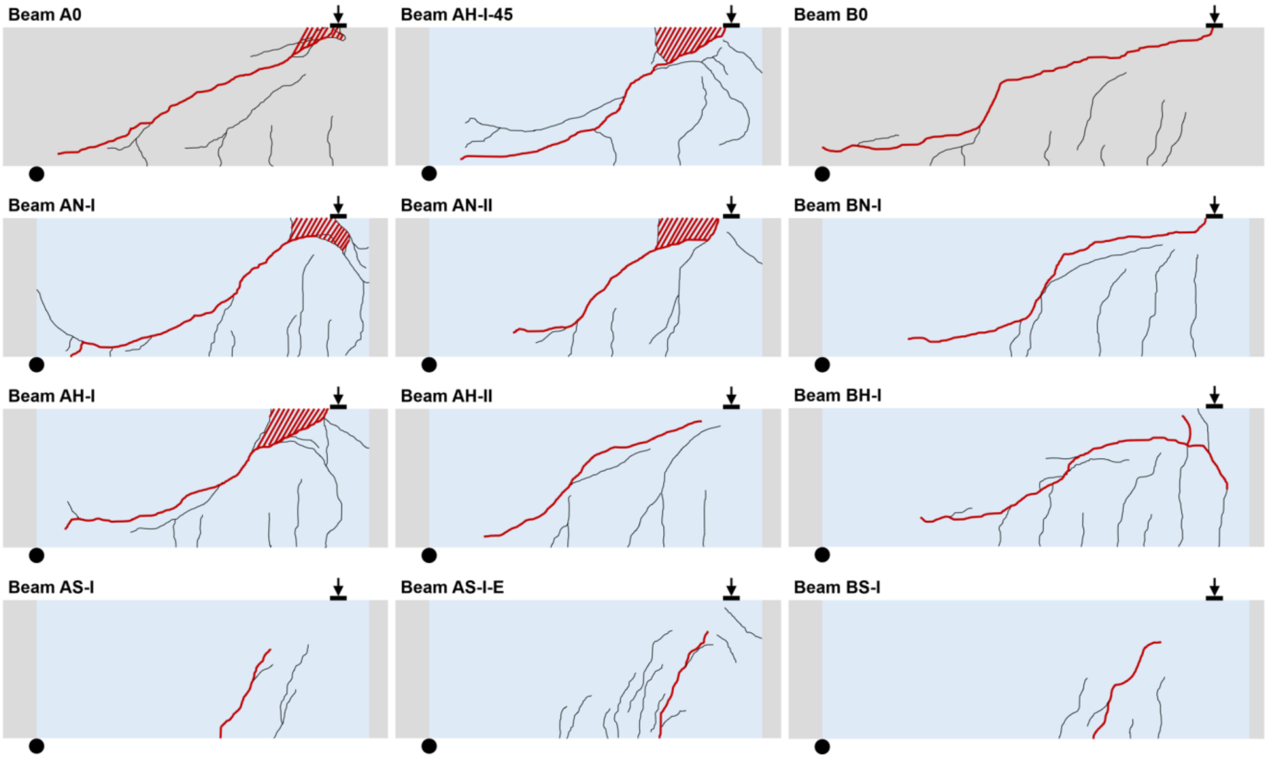

Fig. 7 Crack patterns and failure modes of FRGM-strengthened concrete beams at the ultimate stage.

3.3 Development of crack width

The maximum crack width *vs.* load and deflection relations of the tested specimens are presented in **Fig. 8** and **Fig. 9**, respectively, which were obtained from the DIC results according to the method in [92, 93, 94]. The measured crack was the critical diagonal crack. It should be noted that 30 locations were selected along the diagonal cracks, and the presented crack width at each load or deflection level was calculated as the maximum value among the 30 crack width values. The crack width was compared in three groups (i.e., **Fig. 8a-c** and **Fig. 9a-c**). Generally, the shapes of the curves were similar and could be divided into two stages. Taken AN-II in **Fig. 8a**, for example, at the initial loading stage, the crack width was maintained at the level of zero until the load reached around 160 kN. Then, the diagonal crack emerged, and a non-linear increase in the maximum crack width could be observed. With the increment of the load level, the slope of the curve also increased.

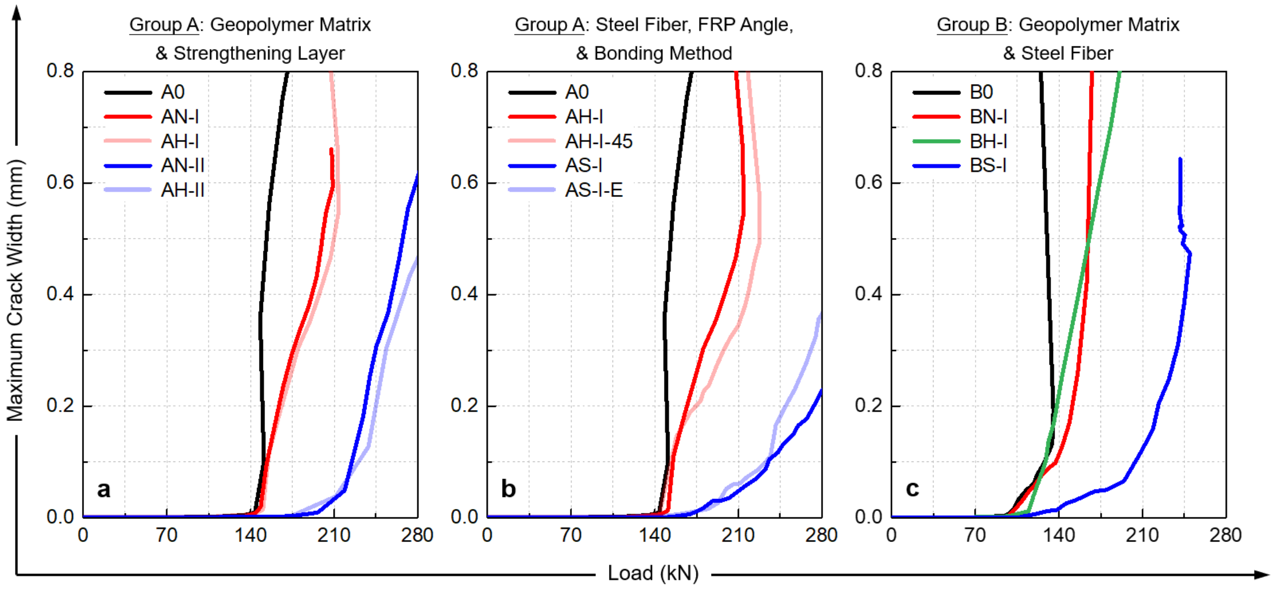

Fig. 8 Maximum crack width *vs.* load relations.

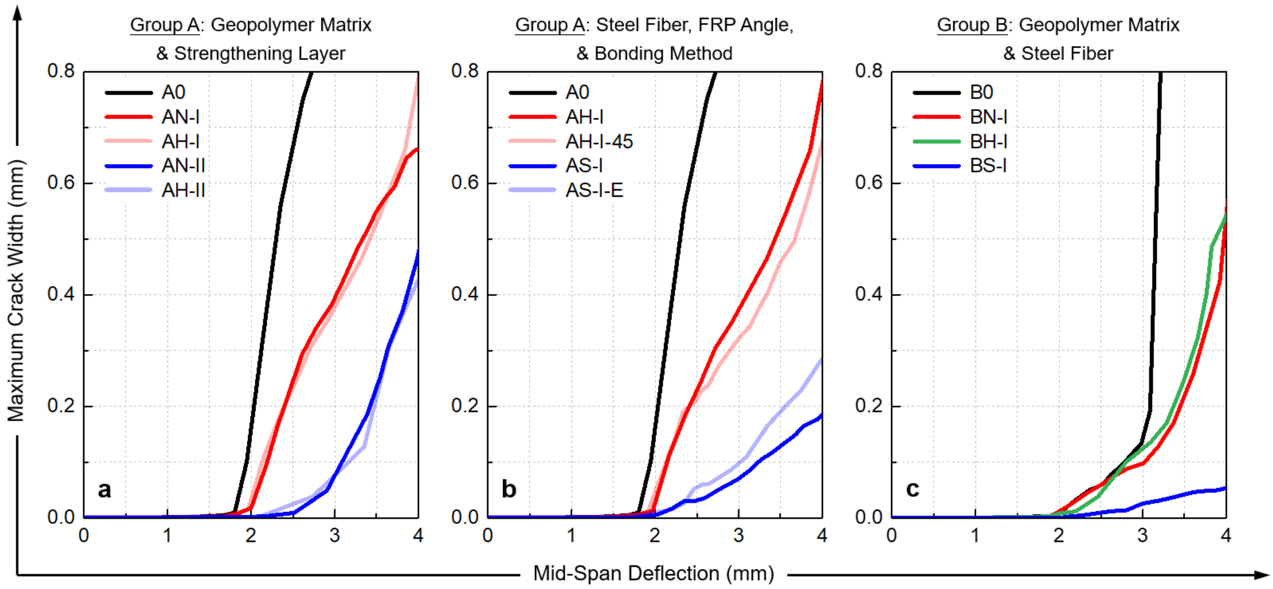

Fig. 9 Maximum critical shear crack width *vs.* deflection relations.

From the curves in **Fig. 8a** and **Fig. 9a**, it can be found that with the increase in the number of the strengthened layer, the width of the critical diagonal crack decreased. At the mid-span deflection of 3 mm, the control specimen (i.e., A0) had a maximum crack width larger than 0.8 mm, while the maximum crack widths of the specimens with one FRGM layer (i.e., AH-I) and two FRGM layers were 0.4 mm and 0.08 mm, respectively. In addition, the slag-to-fly ash ratio of the geopolymer matrix had the minimal effect on the development of the maximum crack width.

In **Fig. 8b** and **Fig. 9b**, it can be found that the direction of the small-diameter CFRP bars slightly affected the maximum crack width. The specimen with vertically (90°)-placed small-diameter CFRP bars (i.e., AH-I) showed a larger maximum crack width than the specimen with 45°-placed small-diameter CFRP bars (i.e., AH-I-45). By adding steel fibers, the maximum crack width could be significantly reduced. At the mid-span deflection of 3 mm, the specimen with 2% steel fiber in the geopolymer matrix (i.e., AS-I) exhibited a maximum crack width smaller than 0.1 mm, while the specimen without the steel fiber (i.e., AH-I) exhibited a maximum crack width of 3.8 mm. In comparison, the bonding methods seemed to show slight influence on the maximum crack width evolution. From **Fig. 9b**, at the initial loading stage (mid-span deflection below 2.5 mm), the geopolymer-bonded specimen (i.e., AS-I) showed a similar maximum crack width with the epoxy-bonded specimen (i.e., AS-I-E). When the deflection was larger than 2.5 mm, the maximum crack width of Beam AS-I-E was larger than that of Beam AS-I.

For the group B specimens (shear span-to-depth ratio of 3.2) in **Fig. 8c** and **Fig. 9c**, the aforementioned phenomena can also be observed, i.e., (1) the strengthened beams had a smaller maximum crack width than the reference beam, (2) slag-to fly ash ratio in geopolymer matrix had a limited effect on the maximum crack width of the strengthened beams; and (3) the maximum crack width could be significantly lowered by adding steel fibers in the geopolymer matrix.

4 Failure processes and DIC results of the tested beams

The failure processes of the beam specimens were analyzed using the DIC technique. Additionally, after the test, the geopolymer matrix around the critical diagonal crack of the beam specimens was removed to observe the in-situ failure modes of small-diameter CFRP bars in the FRGM layer. In the following sub-sections, the DIC strain fields and local failure modes of Beams AH-I, AS-I, AH-I-45, AN-II, and BH-I are presented and discussed in details. In contrast, the failure processes of Beams A0, AN-I, AS-I-E, AH-II, B0, BN-I, and BS-I are summarized in the **Appendix** to improve readability.

4.1 Beam AH-I

Fig. 10 presents the load *vs.* mid-span deflection relationship of Beam AH-I (using geopolymer M-H in the FRGM layer), and the DIC strain fields at four loading stages. Here, the DIC images correspond to the strain fields at the load levels of 72 kN, 145 kN, 217 kN, and 206 kN, respectively. At the load of 72 kN, a vertical flexural crack resulting from the bending load could be observed. At the load of 145 kN, a small shear crack (surrounded by the dashed line in the DIC image of 145 kN) propagated diagonally, and a decrease in the slope of the load-deflection curve could be seen at this stage. When the load reached the peak value (i.e., 217 kN), the critical diagonal crack was observed clearly. Afterwards, the load–deflection curve presented a mild decrease; and during this stage, the width of the diagonal crack and the FRP/geopolymer debonding developed rapidly. After the load of 206 kN, a sudden drop can be observed in the curve. A similar crack pattern was also observed in Beam AN-I using geopolymer M-N as shown in **Fig. A2** of the **Appendix**, which also indicated that the different slag-to-fly ash ratios (AN-I *vs.* AH-I) had little effect on the shear performance of the strengthened beam if the tensile strengths of the formed geopolymer matrix were similar.

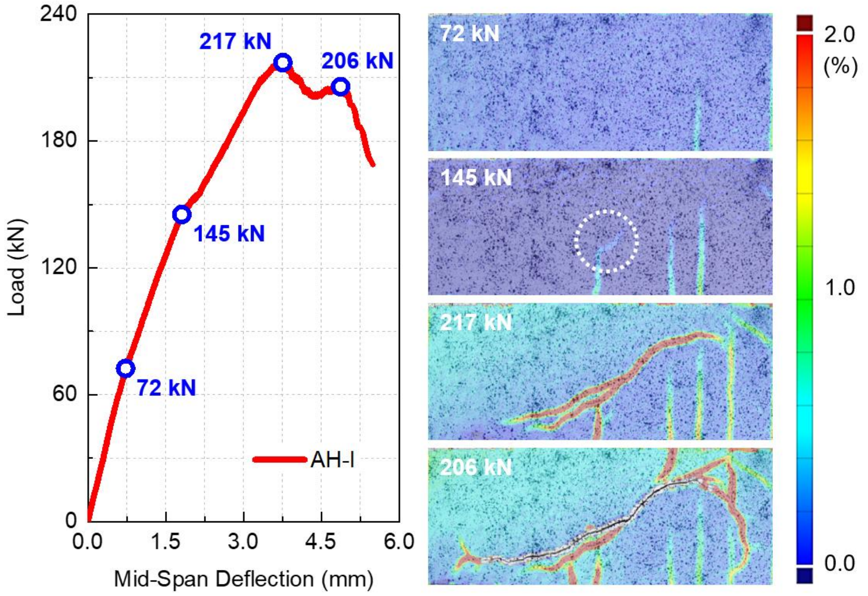

Fig. 10 Failure process and DIC strain fields of Beam AH-I.

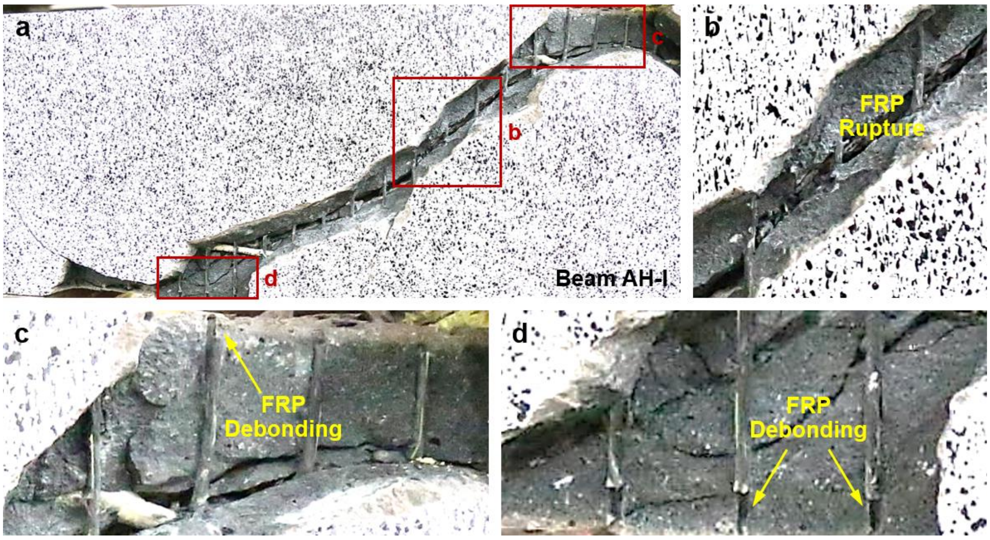

Fig. 11 Local failure mode of the FRGM layer in Beam AH-I: (a) overall view, and the enlarged (b) Window b, (c) Window c, and (d) Window d in **Fig. 11a**.

Fig. 11 presents the final failure mode of the FRGM layer in Beam AH-I. The debonding of the small-diameter CFRP bars could be observed particularly at the two ends of the diagonal crack (see **Fig. 11c** and **Fig. 11d**). The small-diameter CFRP bars also contributed to the shear capacity of the strengthened beam. As the transverse shear strength of the CFRP bar was much lower than its tensile strength [20, 97], the rupture of the small-diameter FRP bar can be seen in **Fig. 11c**. The shear crack in the FRGM layer is almost identical to that in the reference beam A0 in **Fig. A1** of the **Appendix**. For Beam AH-I in **Fig. 11**, the overlapped diagonal cracks of the parent concrete beam and FRGM layer indicated an excellent interaction achieved between the strengthening layer and the RC beam.

4.2 Beam AS-I

Fig. 12 presents the load *vs.* mid-span deflection relation of the beam strengthened with steel fiber-reinforced FRGM layer (AS-I), and the DIC strain fields at three load levels (i.e., 104 kN, 208 kN, and 312 kN). At the load of 104 kN, very fine cracks would be observed at the lower right corner of the DIC image. Compared with the reference beam A0 (in **Fig. A1** of the **Appendix**) and the beam with plain geopolymer matrix (e.g., Beam AH-I in **Fig. 10**), the steel fiber-reinforced FRGM layer showed a superior crack resistance given a similar load level. When the load reached 208 kN, several short slim cracks could be observed at the bottom of the FRGM layer. At the peak load (i.e., 312 kN), it could be seen from the figure that two major flexural/shear cracks were formed (i.e., clearly with a larger slope than those in **Fig. 10**), while the opening of diagonal shear crack appearing at the central beam depth location was suppressed (surrounded by the dashed line). Afterwards, it should be noted that the concrete crushing (i.e., shear-compression failure) was observed at the top of the beam (near the loading point), followed by a sudden load drop. The failure process of the beam strengthened with epoxy-bonded steel fiber-reinforced FRGM layer (i.e., Beam AS-I-E) is shown in **Fig. A3** of the **Appendix**. The load capacities and crack patterns of Beam AS-I and Beam AS-I-E are similar, indicating that the effectiveness of the geopolymer- and epoxy-bonding methods was close.

After the test, the FRGM layer was removed from the strengthened RC beam, and two bonding surfaces (both FRGM and concrete sides) are presented in **Fig. 13**. It is noted that the integrity of the FRGM layer in **Fig. 13a** was well kept due to the addition of steel fibers. It can be seen that a relatively large volume of concrete was attached to the FRGM layer (surrounded by the dashed lines in **Fig. 13a**), indicating an excellent bond between the FRGM layer and concrete substrate. After removing the FRGM layer, the surface of the concrete substrate can be clearly seen in **Fig. 13b**, and a critical diagonal crack can be found in the concrete beam.

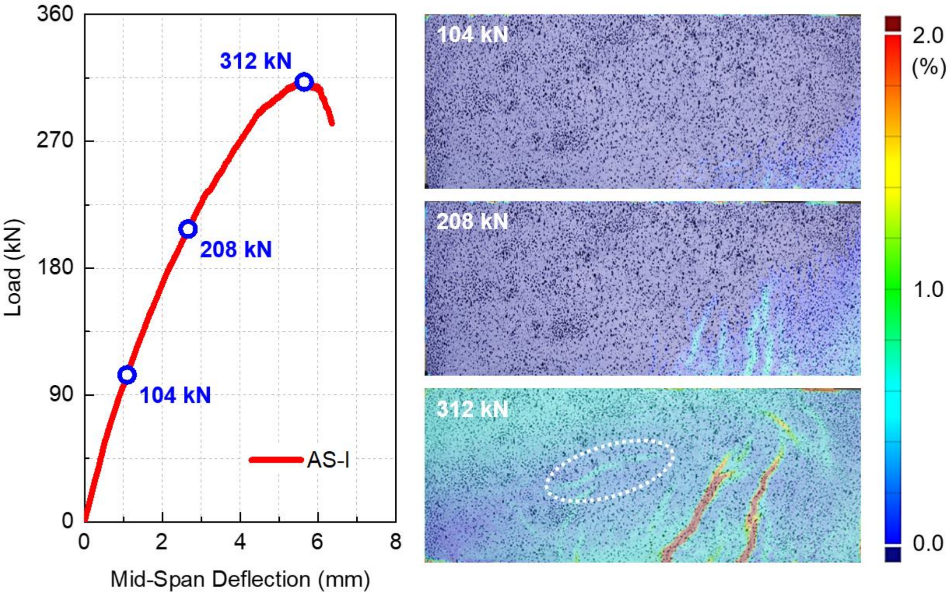

Fig. 12 Failure process and DIC strain fields of Beam AS-I.

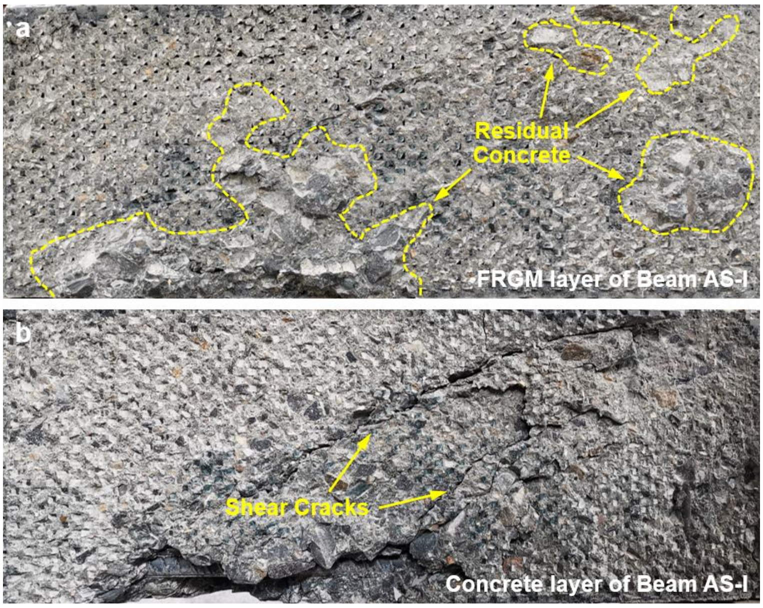

Fig. 13 Bonding surfaces of the (a) FRGM layer and (b) concrete substrate of Beam AS-I.

4.3 Beam AH-I-45

Fig. 14 presents the load *vs.* mid-span deflection relationship of the specimen using 45° small-diameter FRP bars (i.e., Beam AH-I-45), and the DIC strain fields at the load levels of 77 kN, 153 kN, 230 kN, and 215 kN. Similar to Beam AH-I (see **Fig. 10**), the first crack in the shear span approached the mid-span of the beam and propagated vertically. At the load of 153 kN, an arc-shaped diagonal crack was observed. When the load reached peak value (i.e., 230 kN), the governing diagonal crack could be seen while it did not propagate throughout the whole section. Afterwards, the curve of the beam presented a mild decrease, and the diagonal crack developed throughout the entire section. Also, the debonding between the small-diameter CFRP bars and the geopolymer matrix developed rapidly. When the load decreased to 215 kN, the curve presented a sudden drop. In general, the failure process and crack patterns of Beam AH-I-45 were quite similar to those of Beam AH-I in **Fig. 10** (using 90° small-diameter FRP bars), while the load capacity of Beam AH-I-45 was a little higher.

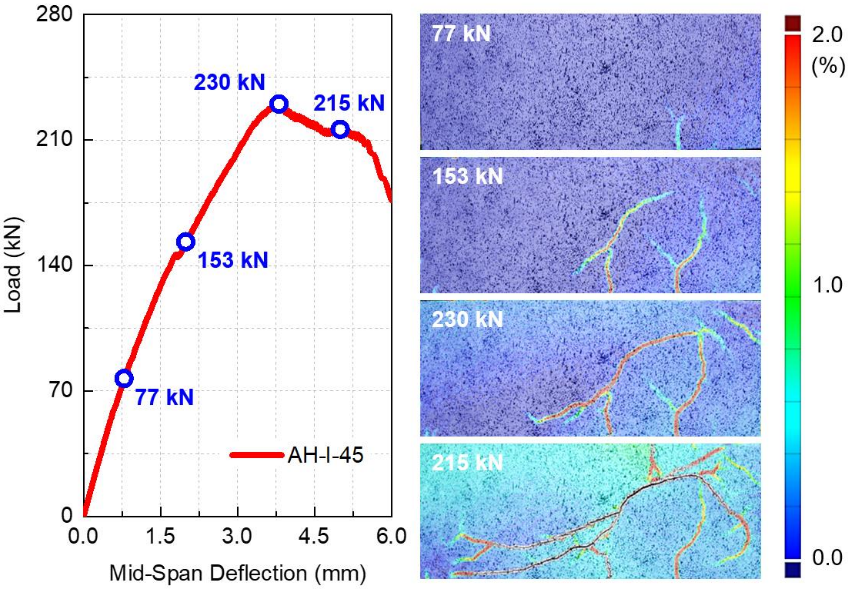

Fig. 14 Failure process and DIC strain fields of Beam AH-I-45.

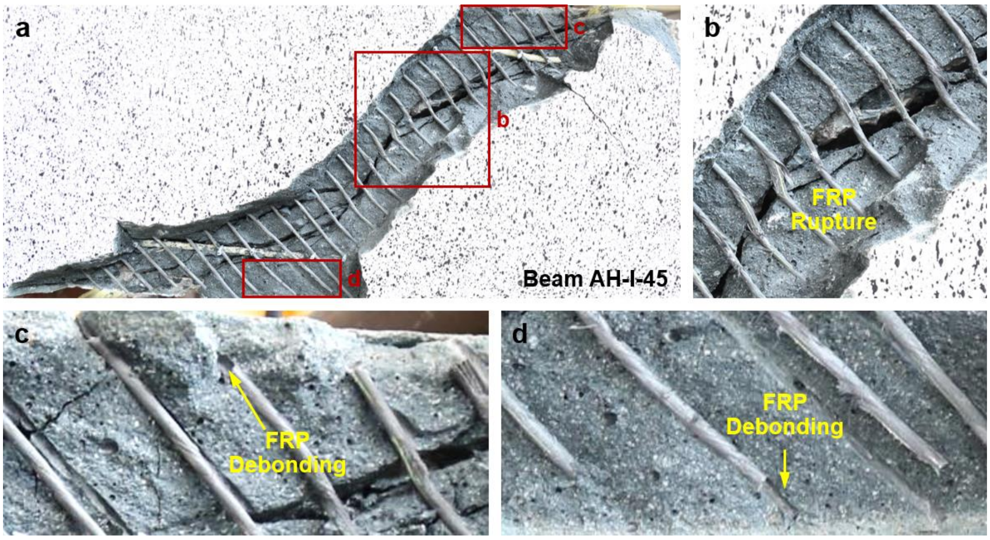

Fig. 15 Local failure mode of the FRGM layer in Beam AH-I-45: (a) overall view, and the enlarged (b) Window b, (c) Window c, and (d) Window d in **Fig. 15a**.

Fig. 15 presented the final failure mode of Beam AH-I-45, which is similar to that of Beam AH-I in **Fig. 11**. The debonding of the small-diameter FRP bars could be seen at both ends of the diagonal crack (see **Fig. 15c** and **Fig. 15d**), owing to the comparatively short embedded length of the small-diameter bar at the debonding side. Additionally, in the middle portion of the diagonal crack, shear rupture failure of small-diameter FRP bars could be observed (see **Fig. 15b**), because the embedded lengths of both ends of the small-diameter bar were large enough. The shear failure of the small-diameter FRP bars also indicated that the FRGM layer was fully utilized in Beam AH-I-45.

4.4 Beam AN-II

Fig. 16 presents the load *vs.* mid-span deflection relation of the specimen with double FRGM layers (i.e., Beam AN-II, using geopolymer M-N), and the DIC strain fields at loads of 114 kN, 227 kN, and 341 kN. When the load reached 114 kN, two vertical cracks emerged in the shear span. At the load of 227 kN, apart from the initial two cracks, a diagonal crack could be seen with an arc shape. At the ultimate stage (i.e., 341 kN), the arc-shaped diagonal crack had the largest width, and the specimen showed a shear-compression failure. In addition, **Fig. 17** presents the final failure mode of the specimen, which is very similar to the results of Beam AH-I (shown in **Fig. 11**) and AH-I-45 (shown in **Fig. 15**). It should be pointed out that the similar failure process was also observed for Beam AH-II using geopolymer M-H, which can be found in **Fig. A4** of the **Appendix**.

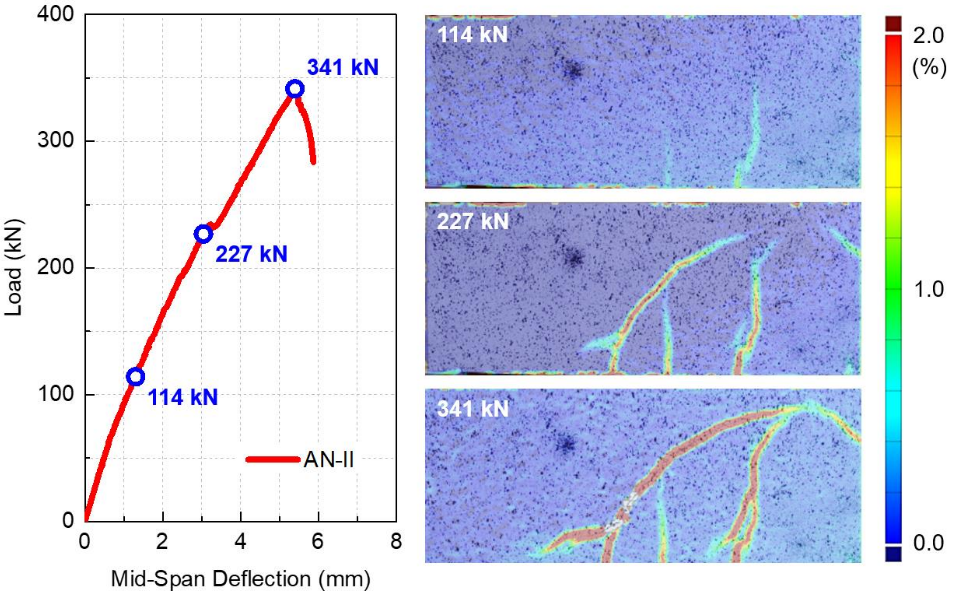

Fig. 16 Failure process and DIC strain fields of Beam AN-II.

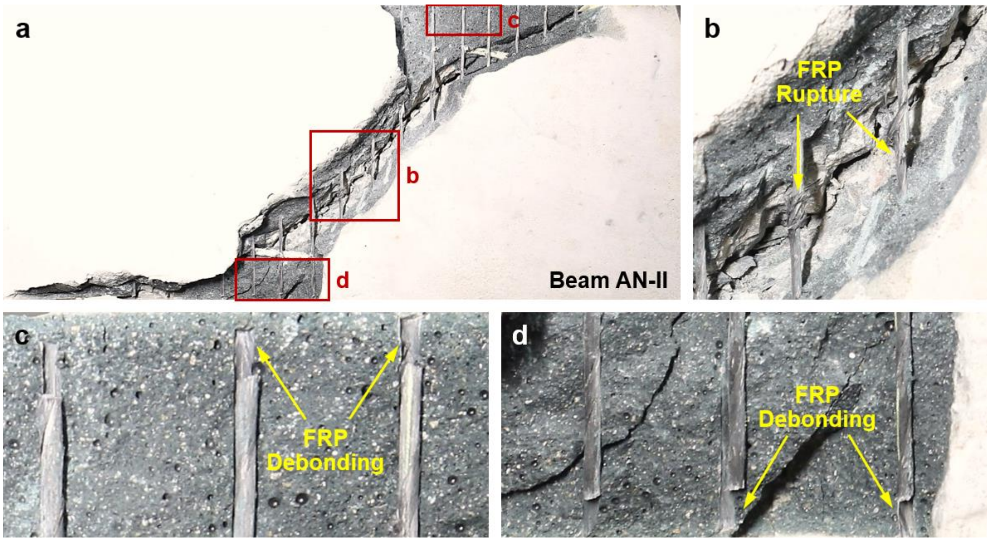

Fig. 17 Local failure mode of the FRGM strengthening layer in Beam AN-II: (a) overall view, and the enlarged (b) Window b, (c) Window c, and (d) Window d in **Fig. 17 a**.

4.5 Beam BH-I

Fig. 18 shows the load *vs.* mid-span deflection relationship of the specimen with the shear span-to-depth ratio of 3.2 (i.e., Beam BH-I), and the DIC strain fields at loads of 67 kN, 134 kN, 201 kN, and 189 kN, respectively. When load reached 67 kN, the vertical cracks in the shear span could be seen. Then, at the load of 134 kN, a diagonal crack appeared together with several vertical cracks. When the load reached the peak value (i.e., 201 kN), the critical diagonal crack could be clearly seen with a considerable width. Afterwards, the curve presented a sudden drop followed by a short constant stage. In the meantime, the crack developed towards the loading point and the support. A sudden drop could be seen on the curve when the load decreased to 189 kN, indicating the complete failure of the specimen. **Fig. 19** presents the final failure mode of Beam BH-I, in which the observations were similar to those of Beam AH-I in **Fig. 11**. It is noted that the failure processes of the other specimens in group B (i.e., B0, BN-I, and BS-I) can be found in **Fig. A5**, **Fig. A6**, and **Fig. A7** of the **Appendix**. In addition, the findings obtained from the specimens in group B (i.e., B0, BN-I, BH-I, and BS-I) are similar to those obtained from the specimens in group A (i.e., A0, AN-I, AH-I, and AS-I), in terms of the effects of slag-to-fly ash ratios and steel fiber reinforcements on the strengthened beams.

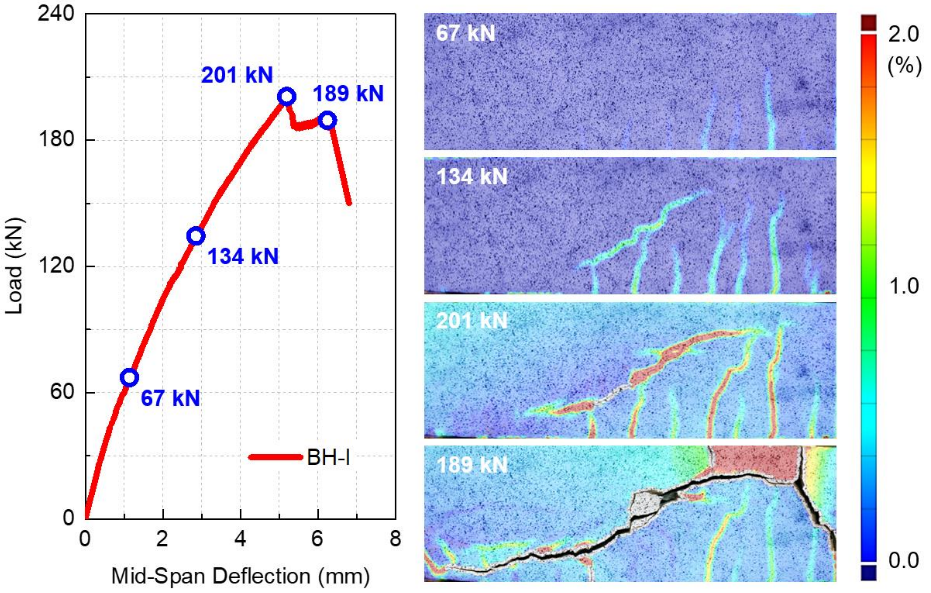

Fig. 18 Failure process and DIC strain fields of Beam BH-I.

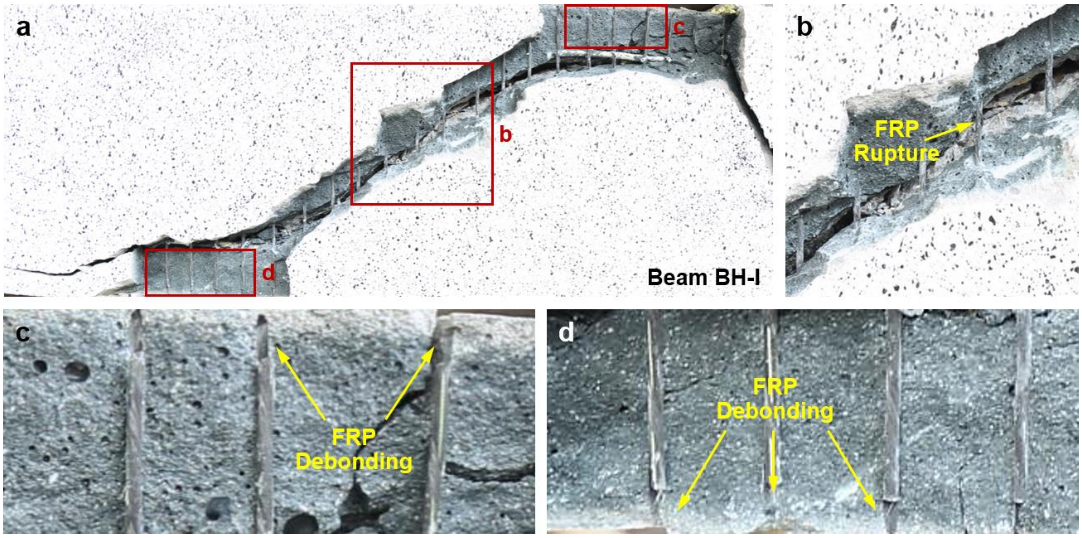

Fig. 19 Local failure mode of the FRGM layer in Beam BH-I: (a) overall view, and the enlarged (b) Window b, (c) Window c, and (d) Window d in **Fig. 19a**.

4.6 Summary of load-carrying mechanism of the strengthened beams

Based on the experimental findings, the load-carrying mechanism of the FRGM-strengthened beams could be summarized as follows. At the initial loading stage, since the FRGM layer was well bonded with the RC beam, the initial shear force was mainly carried by the concrete of RC beam and the geopolymer matrix of FRGM layer. Herein, a compression path would be formed from the loading point to the support. Meanwhile, the internal tensile force was perpendicular to the formed compression path. Once the internal tensile force reached the tensile strength of concrete and the geopolymer matrix, the diagonal crack would initiate and propagate, and the internal tensile force carried by concrete and geopolymer matrix would be transferred to the FRP bars. After the rupture of the FRP bars, the strengthened beam failed. Therefore, the strength of concrete and the geopolymer matrix would greatly influence the load point when the diagonal crack initiated. In addition, the design of the FRP rebar (e.g., inclination and reinforcement ratio) would mainly influence the load carrying capacity and the slope of the load-deflection curve after diagonal crack formed.

4.7 Effective strain of small-diameter CFRP bar

The shear failure of RC beams mostly occurs with a diagonal tension crack. The crack usually starts with the vertical flexural cracks from the tensile face of RC beams, and then develops towards the loading point. Cheng and Teng [17, 18] mentioned that the strain distribution in the FRP reinforcement along the shear crack is non-uniform. The strains of FRP bars in the strengthened RC beam intersected by the diagonal crack are strongly affected by the crack width due to the linear elastic behavior of FRP. The maximum strain in the FRP reinforcement can be reached with the increasing width of the diagonal crack.

However, it is difficult to use the conventional method (i.e., attaching strain gauges on the surface of FRP reinforcement) to measure the actual strain distribution in small-diameter CFRP bars along the diagonal crack during the test because the position of the crack is difficult to predict, and the shear failure process of the RC beam is brittle. For the present test, the DIC analysis was used to monitor the strain field and cracking behavior of the strengthened RC beams.

According to the DIC results, it is assumed that the debonding between small-diameter CFRP bars and geopolymer matrix was comparatively small at the peak load, because the critical shear crack opening at the peak load were well-restrained by the geopolymer mortar, and significant debonding occurred only after the peak load. As the local debonding between small-diameter CFRP bars and geopolymer mortar was difficult to monitor from the DIC results, it is assumed here that FRP bars were well bonded to the geopolymer matrix. The strains in small-diameter CFRP bars can be estimated from the DIC results by calculating the strain of geopolymer at the position of each small-diameter FRP bar. Afterwards, the effective strain of CFRP bars (**Table 4**) in the FRGM strengthening layer can be determined by averaging the obtained strains in each small-diameter CFRP bars. It should be pointed out that only the small-diameter CFRP bars intersected by the diagonal shear crack and distributed within the beam's effective depth were used to determine the effective strain.

Table 4 presents the peak load, the corresponding mid-span deflection, and the effective strains of the small-diameter CFRP bars. From the table, it can see that (1) The compressive strength of geopolymer mortar had marginal effect on the effective strain of small-diameter CFRP bars in this study (2830 $\mu\varepsilon$ in AN-II and 3160 $\mu\varepsilon$ in AH-II; 1890 $\mu\varepsilon$ in AN-I and 1820 $\mu\varepsilon$ in AH-I). (2) The use of the CFRP bars distributed at 45° to the beam's longitudinal axis could provide higher effective strain in CFRP bars compared to the CFRP bars distributed perpendicularly to the longitudinal axis (i.e., 1890 $\mu\varepsilon$ in AN-I, 1820 $\mu\varepsilon$ in AH-I and 2220 $\mu\varepsilon$ in AH-I-45). (3) With the increase on the number of the FRGM strengthening layers, the effective strain of small-diameter CFRP bar increased, owing to the larger deformation and ultimate load of the specimen, the effective strain of small-diameter CFRP bars in AH-II could be 1.7 times that in AH-I. (4) Through adding steel fibers into the geopolymer mortar, the effective strain of the small-diameter CFRP bar decreased. Here, AS-I and AS-I-E seemed to present comparable ultimate loads and mid-span deflections with AN-II and AH-II, while the effective strain of small-diameter CFRP bars in the steel fiber reinforced geopolymer was only about 50% of those in AN-II and AH-II. It may be related to the debonding between the FRGM layer and the concrete substrate during the loading process (**Fig. 13**), leading to the deformation incompatibility between the FRGM and RC layers. (5) With the increase of the shear span-to-depth ratio, the effective strain of small-diameter FRP bar slightly increased due to the shift of shear compression failure to diagonal tension failure.

Table 4 The average tensile strain of small-diameter CFRP bars in beams at the peak load.

Specimen ID	Peak Load (kN)	Mid-Span Deflection (mm)	Average Tensile Strain of FRP (με)
A0	181	2.91	/
AN-I	210	3.89	1890
AN-II	341	5.40	2830
AH-I	217	3.78	1820
AH-II	353	5.69	3160
AH-I-45	230	3.80	2220
AS-I	312	5.63	1440
AS-I-E	319	5.61	1540
B0	136	3.08	/
BN-I	179	5.36	1970
BH-I	201	5.21	2470
BS-I	252	6.71	1820

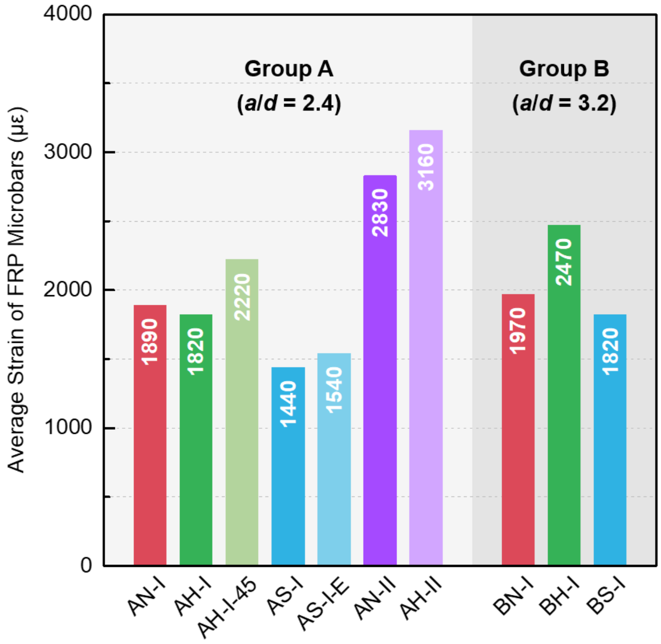

Fig. 20 Average strain of small-diameter FRP bars. The FRP's average strains of the double-side strengthened beam specimens are larger than those of the single-side strengthened specimens.

5 Theoretical analyses

This section presents the prediction method for the shear capacities of the FRGM-strengthened RC beams. The shear capacity of the FRGM strengthened RC beams, V_S, is contributed by two parts: i.e., from the original RC beam (V_{RC}) and the FRGM strengthening layer(s) (V_{FRGM}) as illustrated in **Eq. (1)**.

$$V_S = V_{RC} + V_{FRGM} \tag{1}$$

where the shear capacity of the un-strengthened RC beam V_{RC} is contributed by concrete and transverse reinforcement, which can be predicted using the classical model [100] adopted in ACI PRC-445-99 [101].

$$V_{RC} = \begin{cases} \left[2.21 \left(f_c' \rho_s \dfrac{h_0}{a} \right)^{1/3} \right] \left(\dfrac{2.5 h_0}{a} \right) b_w h_0 & (a/h_0 \le 2.5) \\ 2.21 \left(f_c' \rho_s \dfrac{h_0}{a} \right)^{1/3} b_w h_0 & (a/h_0 > 2.5) \end{cases} \tag{2}$$

in which f'_c is the compressive strength of concrete used in the RC beam; ρ is the flexural steel reinforcement ratio; b_w, h_0, and a are the width, effective depth, and span length of RC beams, respectively.

The shear contribution of the FRGM layer (V_{FRGM}) in the strengthened beams is from two parts: the geopolymer matrix (V_G) and FRP reinforcement (V_{FRP}). According to the experimental design, three types of geopolymer (i.e., plain geopolymer M-N and M-H, and steel fiber-reinforced geopolymer M-S) were used in the FRGM strengthening layer. As very limited work could be found on the shear performance of fiber-reinforced geopolymer, the shear capacities of the plain and fiber-reinforced geopolymer were estimated based on the equation for fiber-reinforced concrete proposed by Khuntia et al. [102]. The shear capacity of the geopolymer (V_G) in the FRGM layer can be calculated as **Eq. (3)**.

$$V_G = v_G b_{FRGM} h_0 \tag{3}$$

where b_{FRCM} is the thickness of the FRGM layer; h_0 is the effective depth of the RC beam. The parameter v_G is the shear strength of the geopolymer mortar which can be obtained by **Eq. (4)**.

$$v_G = \begin{cases} \left[0.167 \left(2.5 \dfrac{h_0}{a} \right) + 0.25F \right] \sqrt{f_G'} & (a/h_0 \le 2.5) \\ (0.167 + 0.25F) \sqrt{f_G'} & (a/h_0 > 2.5) \end{cases} \tag{4}$$

where f'_G is the cylinder compressive strength of the geopolymer mortar; h_0 and a are the effective depth and span length of RC beams, respectively. In this study, the cylinder compressive strength of geopolymer (Φ100 mm × 200 mm) was measured at 28 d, and the results of geopolymer M-N, M-H, and M-S were 71.7 MPa, 87.2 MPa, and 97.0 MPa, respectively. The parameter F is a fiber factor defined by **Eq. (5)**.

$$F = (L_f / D_f) V_f d_f \tag{5}$$

where L_f and D_f are the length and diameter of the steel fiber, respectively; V_f is the volume fraction of steel fiber in matrix; and d_f is the bond factor which is defined as 0.5, 0.75, and 1.00 for round fibers, crimped fibers, and indented fibers, respectively.

According to the existing analysis models [17, 18, 97, 98] for determining the shear capacity of FRP-strengthened RC beams, the shear strength contributed by the FRP reinforcement can be expressed by **Eq. (6)**.

$$V_{FRP} = n \varepsilon_{FRP} E_{FRP} A_{FRP} \frac{h_{FRP} (\cot\theta + \cot\beta) \sin\beta}{S_{FRP}} \tag{6}$$

where n, A_{FRP}, ε_{FRP}, E_{FRP}, and h_{FRP} are the number of layers, cross-sectional area, effective strain, elastic modulus, and effective depth of the FRP reinforcement, respectively; θ is the angle between the diagonal shear crack and the longitudinal beam axis (**Fig. 21**); β is the angle between the beam's longitudinal axis and small-diameter CFRP bars (**Fig. 21**); and S_{FRP} is the space between small-diameter CFRP bars. The effective depth h_{FRP} of small-diameter CFRP bars is defined as $0.9h_0$ (**Fig.**

21) [17, 18], where h_0 is the effective depth of the RC beam.

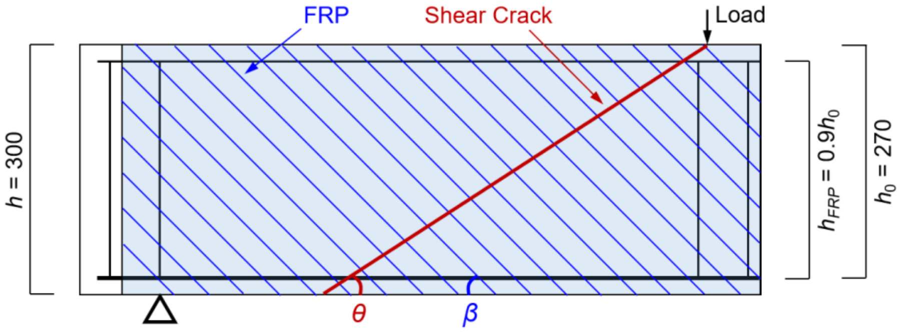

Fig. 21 Directions of the governing shear crack and FRP bars of the FRGM layer.

According to the experimental results (**Fig. 7**), the diagonal shear crack angle θ is assumed as 45° for all strengthened RC beams. Furthermore, it is assumed that there is no debonding occurred between small-diameter CFRP bars and geopolymer mortar before the peak load of the strengthened RC beam. It should be pointed out that the effective strain of the CFRP bars would be overestimated in this simplification, as slight debonding still occurred before the peak load. The effective strain of CFRP reinforcement ε_{FRP} (**Table 4**) used in the FRGM strengthening layer can be determined by averaging the strain in the small-diameter CFRP bars, which was obtained from the DIC results as discussed in ***Section 4.6***. Accordingly, for predicting the shear capacity of FRGM-strengthened RC beams (V_S), the following formula can be derived.

$$V_S = V_{RC} + V_G + V_{FRP} \tag{7}$$

The predicted shear capacities of all the FRGM-strengthened RC beams are listed in **Table 5**, and the comparison of the experimental and predicted results are shown in **Fig. 22**. It can be seen that the predicted shear capacity is in an acceptable agreement with the experimental results. It should be pointed out that the predicted shear capacities of the strengthened RC beams with the steel fiber-reinforced geopolymer were lower than the experimental values. The possible reason for this phenomenon may be that **Eq. (3)** is used to predict the shear capacity of steel fiber reinforced conventional concrete, and the actual shear capacity of steel fiber-reinforced geopolymer may be higher than that of conventional concrete. As this study is the first trial to investigate the shear performance of the FRGM-strengthened RC beams, the experimental data is still very limited. In the future studies, the afore-mentioned method should be further checked or updated based on extended database.

Table 5 Comparison of the experimental results (V_{EXP}) and the predicted results (V_S).

Specimen	V_{RC} (kN)	V_G (kN)	V_{FRP} (kN)	V_S (kN)	V_{EXP} (kN)	Variation (%)
A0	82	/	/	82	91	-9.7
AN-I	82	14	20	115	105	9.6
AH-I	82	15	19	116	109	6.7
AN-II	82	27	59	168	171	-1.4
AH-II	82	30	66	178	177	0.7
AH-I-45	82	15	33	130	115	12.6
AS-I	82	31	15	127	156	-18.3

AS-I-E	82	31	16	128	160	-19.4
B0	71	/	/	71	68	4.8
BN-I	71	13	21	105	90	17.2
BH-I	71	14	26	111	101	10.9
BS-I	71	29	19	119	126	-5.7

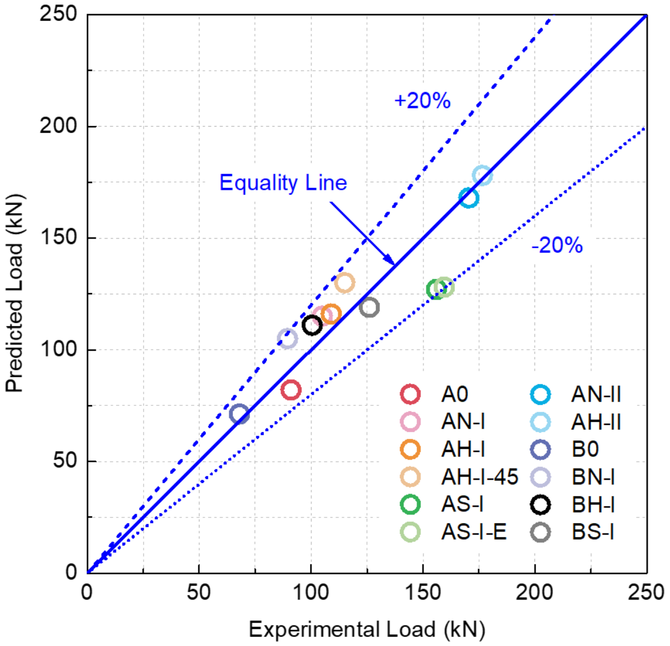

Fig. 22 Comparison of the experimental results and the predicted results.

6 Conclusions

In this study, an experimental program was carried out to investigate the structural performance of RC beams shear strengthened with small-diameter CFRP bar-reinforced geopolymer matrix (FRGM). According to the test results and discussions, the following conclusions can be obtained.

- The RC beams strengthened with the FRGM system exhibited significantly higher ultimate loads than the reference beam. The strengthening efficiency of RC beams with the double-side bonded FRGM layer (1.9 times that of the reference beam) was much larger than that of the RC beams with the single-side bonded FRGM layer (1.2 times that of the reference beam).

- The overall interfacial debonding between the RC beams and the FRGM strengthening layer was not observed in the strengthened RC beams in spite of the occurrence of local debonding between the small-diameter CFRP bars and the geopolymer matrix. The RC beam strengthened with the geopolymer-bonded (cast-in-place) FRGM layer showed a similar load-deflection behavior and failure mode with its epoxy-bonded counterpart, indicating that the strengthening efficiency of the geopolymer-bonding method was acceptable. Particularly, the load capacity of geopolymer-bonded FRGM-RC beam was 98% of that of epoxy-bonded counterpart.

- The small-diameter CFRP bars placed at 45° to the RC beams' longitudinal axis in the strengthening layer led to more shear contribution (i.e., 36% higher) than those set at 90° to the RC beams' longitudinal axis. The use of steel fibers in geopolymer mortar could improve the shear contribution of the FRGM in the strengthened RC beams due to the crack restraining effects of the steel fibers in the FRGM layer. The DIC results could explain well the crack formation and failure mechanism of the strengthened RC beams.

- Based on the average strain obtained from DIC analysis, an analytical investigation was conducted to predict the shear capacities of the strengthened RC beams. The experimental and predicted results showed good agreements, which demonstrated the applicability of the analytical model.

It should be noted that this research is the first trial to investigate the structural performance of RC beams shear strengthened with the geopolymer-bonded small-diameter FRP bar system. As only one beam of each group was adopted in the study, the reliability of the quantitative and statistical analysis of the reported data should be further studied in the future research. It is worth mentioning that the flexural strengthening of RC beams using the same system has also been investigated by the authors and the results can be found in [79].

Acknowledgments

This study was supported by Chinese Guangdong Province R&D Plan for Key Areas (Project Code: 2019B111107002) and Hong Kong-Guangzhou Technology and Innovation Partnership Program (Project Code 201807010055). Kai-Di Peng and Ling-Yu Xu acknowledges the Ph.D. studentship offered by The Hong Kong Polytechnic University. Jun-Qi Huang acknowledges the financial support by the National Natural Science Foundation of China (Grant No. 52208158) and the Anhui Provincial Natural Science Foundation (No. 2208085QE172). Bo-Tao Huang acknowledges the support of the Hong Kong Innovation and Technology Fund (Project Code: ITS/077/18FX) through the Research Talent Hub.

Declaration of Competing Interest

The authors declare that they have no known competing financial interests or personal relationships that could have appeared to influence the work reported in this paper.

CRediT Author Statement

KD Peng: Conceptualization, Methodology, Investigation, Data Curation, Writing - Original Draft. **JQ Huang**: Investigation, Data Curation, Writing - Original Draft. **BT Huang**: Conceptualization, Methodology, Visualization, Writing - Review & Editing. **LY Xu**: Validation, Resources. **JG Dai**: Conceptualization, Funding Acquisition, Supervision, Writing - Review & Editing.

Appendix: Failure processes of Beams A0, AN-I, AS-I-E, AH-II, B0, BN-I, and BS-I

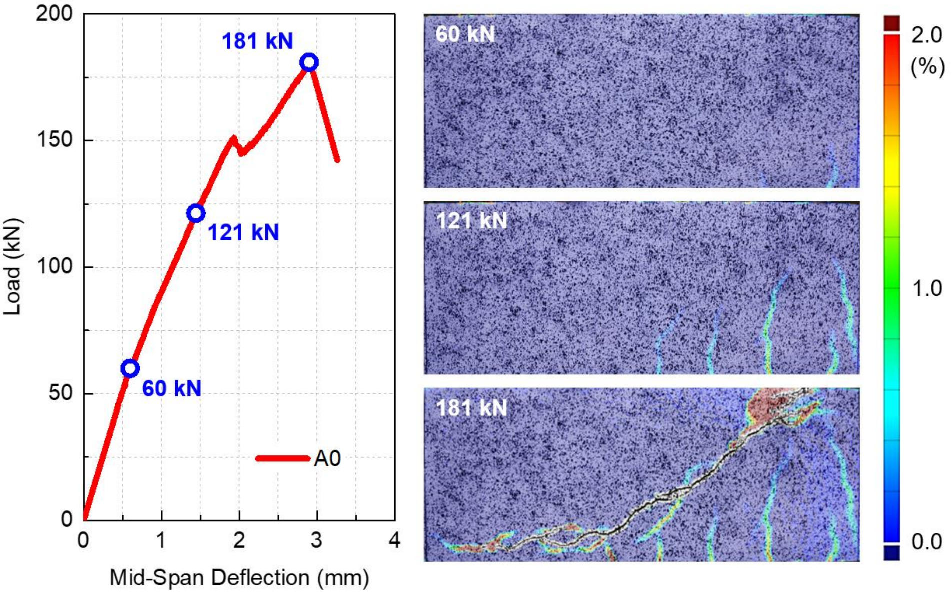

Fig. A1 Failure processes and DIC strain fields of Beam A0.

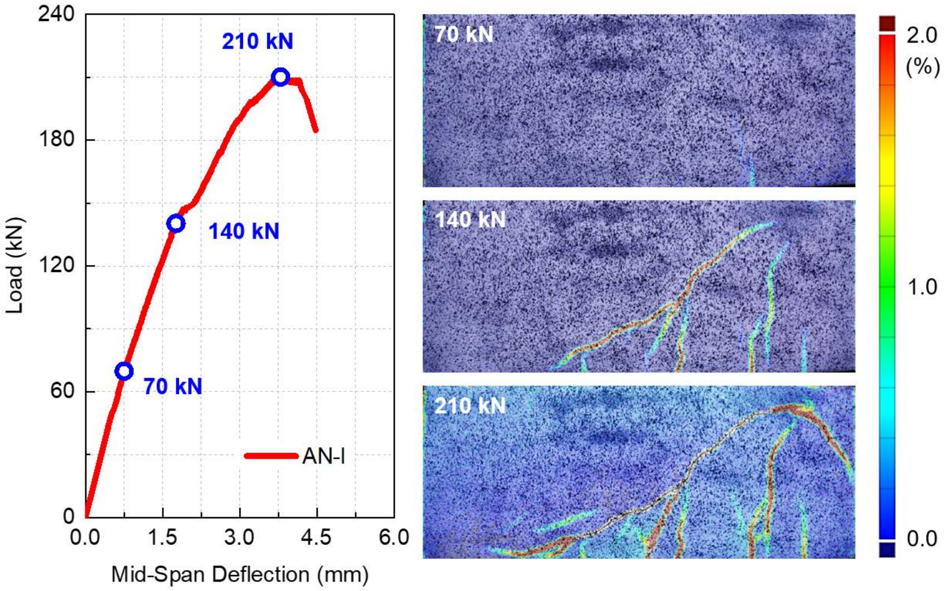

Fig. A2 Failure processes and DIC strain fields of Beam AN-I.

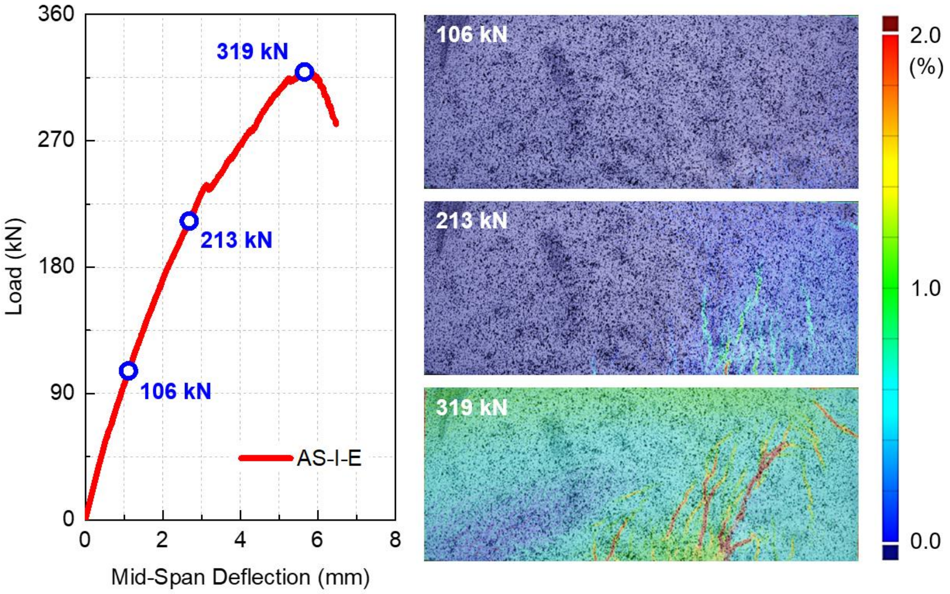

Fig. A3 Failure processes and DIC strain fields of Beam AS-I-E.

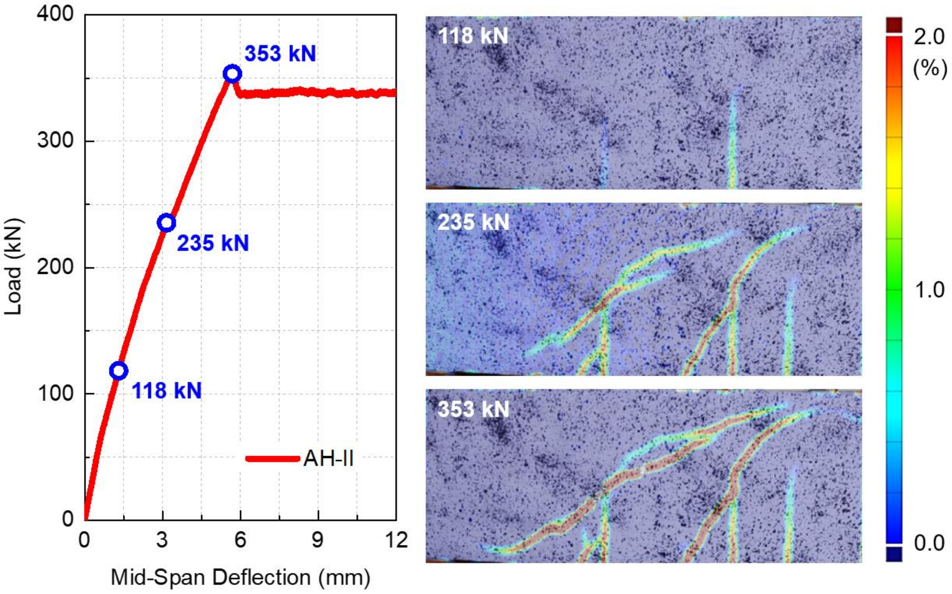

Fig. A4 Failure processes and DIC strain fields of Beam AH-II.

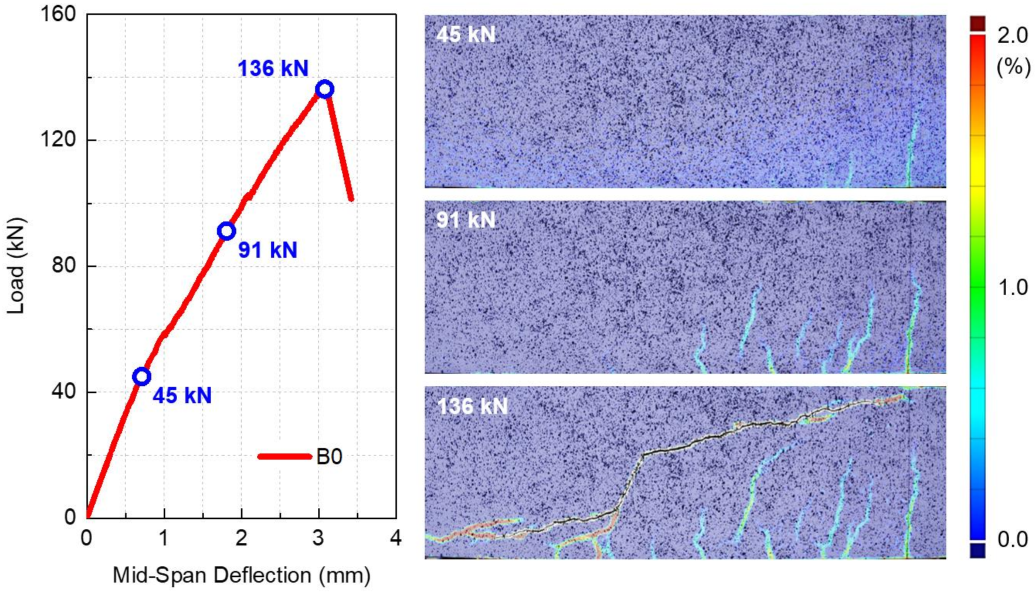

Fig. A5 Failure processes and DIC strain fields of Beam B0.

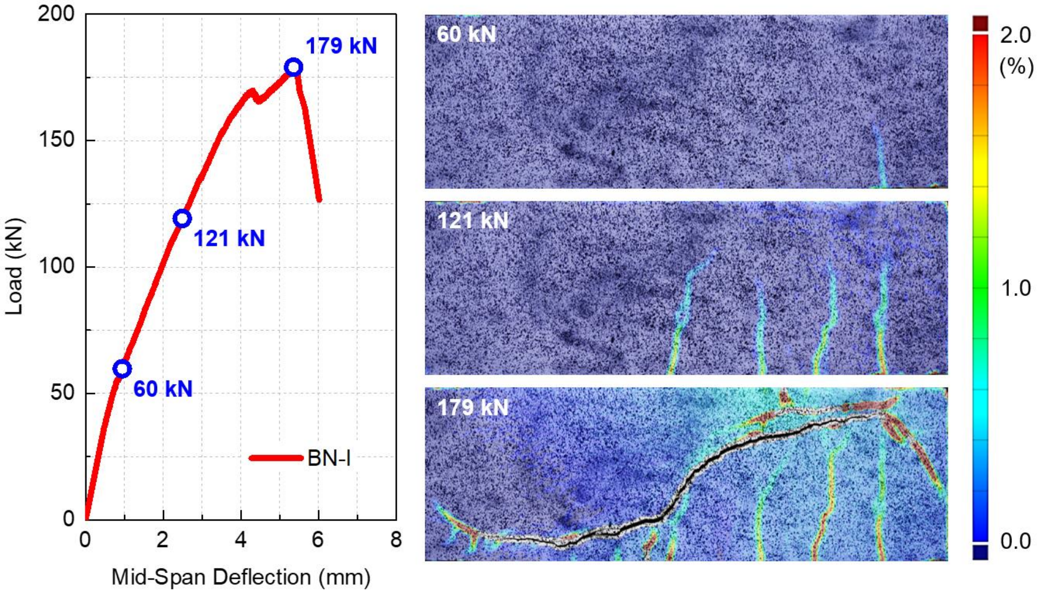

Fig. A6 Failure processes and DIC strain fields of Beam BN-I.

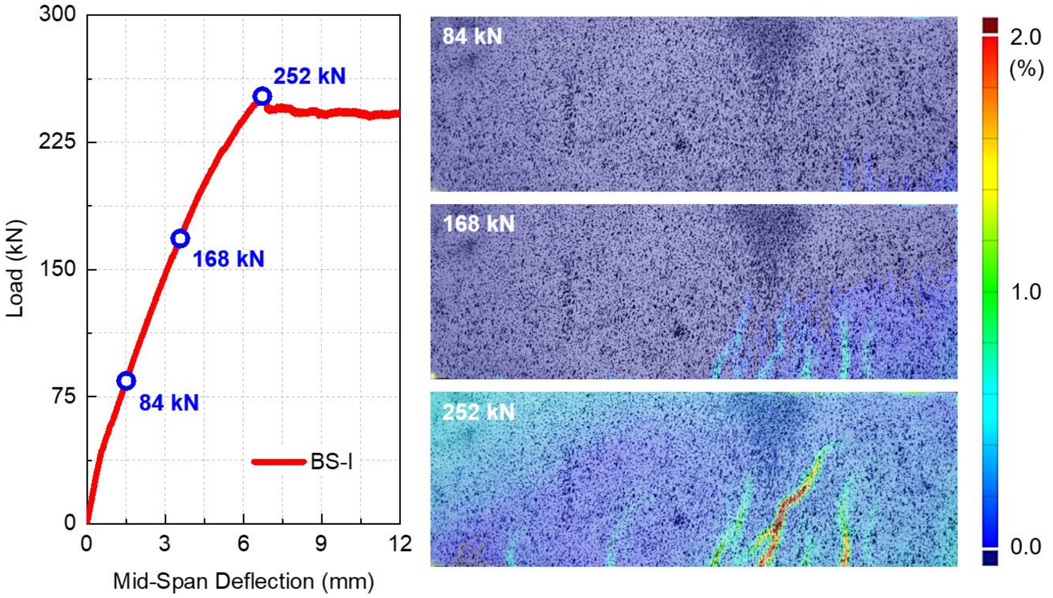

Fig. A7 Failure processes and DIC strain fields of Beam BS-I.

References

1. Neville, A. M., & Brooks, J. J. (1987). Concrete technology (Vol. 438). England: Longman Scientific & Technical.
2. Huang, B. T., Dai, J. G., Weng, K. F., Zhu, J. X., & Shah, S. P. (2021). Flexural Performance of UHPC–Concrete–ECC Composite Member Reinforced with Perforated Steel Plates. Journal of Structural Engineering, 147(6), 04021065.
3. Li, S., Chan, T. M., & Young, B. (2022). Mechanical analysis and finite element modeling of FRP-ECC-HSC composite stub column under axial compression. Journal of Building Engineering, 62, 105212.
4. Yin, X., Li, Q., Xu, X., Chen, B., Guo, K., & Xu, S. (2022). Investigation of Continuous Surface Cap Model (CSCM) for Numerical Simulation of Strain-Hardening Fibre-Reinforced Cementitious Composites against Low-Velocity Impacts. Composite Structures, 116424. DOI: 10.1016/j.compstruct.2022.116424
5. Anas, S. M., Alam, M., & Umair, M. (2021). Performance of one-way concrete slabs reinforced with conventional and polymer re-bars under air-blast loading. In Chandrasekaran S., Kumar S., Madhuri S. (eds) Recent Advances in Structural Engineering. Lecture Notes in Civil Engineering, 135, 179-191.
6. Anas, S. M., Alam, M., & Umair, M. (2022). Air-blast and ground shockwave parameters, shallow underground blasting, on the ground and buried shallow underground blast-resistant shelters: a review. International Journal of Protective Structures, 13(1), 99-139.
7. Anas, S. M., Alam, M., & Umair, M. (2021). Experimental and numerical investigations on performance of reinforced concrete slabs under explosive-induced air-blast loading: a state-of-the-art review. Structures, 31, 428-461.
8. Anas, S. M., Alam, M., & Umair, M. (2022). Performance based strengthening with concrete protective coatings on braced unreinforced masonry wall subjected to close-in explosion. Materials Today: Proceedings, 64, 161-172.
9. Teng, J. G., Chen, J. F., Smith, S. T., & Lam, L. (2002). FRP: strengthened RC structures. John Wiley & Sons, UK.
10. Smith, S. T., & Teng, J. G. (2002). FRP-strengthened RC beams. I: review of debonding strength models. Engineering Structures, 24(4), 385-395.

11. Su, M. N., Wei, L., Zhu, J. H., Ueda, T., Guo, G. P., & Xing, F. (2019). Combined impressed current cathodic protection and FRCM strengthening for corrosion-prone concrete structures. Journal of Composites for Construction, 23(4), 04019021.
12. Smith, S. T., & Teng, J. G. (2002). FRP-strengthened RC beams. I: review of debonding strength models. Engineering structures, 24(4), 385-395.
13. Yang, X., Gao, W. Y., Dai, J. G., Lu, Z. D., & Yu, K. Q. (2018). Flexural strengthening of RC beams with CFRP grid-reinforced ECC matrix. Composite Structures, 189, 9-26.
14. Huang, B. T., Li, Q. H., Xu, S. L., & Zhang, L. (2019). Static and fatigue performance of reinforced concrete beam strengthened with strain-hardening fiber-reinforced cementitious composite. Engineering Structures, 199, 109576.
15. Huang, B. T., Li, Q. H., Xu, S. L., & Zhou, B. (2019). Strengthening of reinforced concrete structure using sprayable fiber-reinforced cementitious composites with high ductility. Composite Structures, 220, 940-952.
16. Li, Q., Yin, X., Huang, B., Zhang, Y., & Xu, S. (2022). Strengthening of the concrete face slabs of dams using sprayable strain-hardening fiber-reinforced cementitious composites. Frontiers of Structural and Civil Engineering, 16(2), 145-160.
17. Chen, J. F., & Teng, J. G. (2003). Shear capacity of fiber-reinforced polymer-strengthened reinforced concrete beams: Fiber reinforced polymer rupture. Journal of Structural Engineering, 129(5), 615-625.
18. Chen, J. F., & Teng, J. G. (2003). Shear capacity of FRP-strengthened RC beams: FRP debonding. Construction and Building Materials, 17(1), 27-41.
19. Younis, A., Ebead, U., & Shrestha, K. C. (2017). Different FRCM systems for shear-strengthening of reinforced concrete beams. Construction and Building Materials, 153, 514-526.
20. Yang, X., Gao, W. Y., Dai, J. G., & Lu, Z. D. (2020). Shear strengthening of RC beams with FRP grid-reinforced ECC matrix. Composite Structures, 241, 112120.
21. Baggio, D., Soudki, K., & Noel, M. (2014). Strengthening of shear critical RC beams with various FRP systems. Construction and Building Materials, 66, 634-644.
22. Azam, R., & Soudki, K. (2014). FRCM strengthening of shear-critical RC beams. Journal of Composites for Construction, 18(5), 04014012.
23. Khalifa, A., Gold, W. J., Nanni, A., & MI, A. A. (1998). Contribution of externally bonded FRP to shear capacity of RC flexural members. Journal of Composites for Construction, 2(4), 195-202.
24. Li, S., Chan, T. M., & Young, B. (2022). Experimental investigation on axial compressive behavior of novel FRP-ECC-HSC composite short column. Composite Structures, 116285.
25. Li, S., Chan, T. M., & Young, B. (2022). Compressive behavior and analysis-oriented model of FRP-confined engineered cementitious composite columns. Engineering Structures, 270, 114869.
26. Li, S., Chan, T. M., & Young, B. (2022). Behavior of GFRP-concrete double tube composite columns. Thin-Walled Structures, 178, 109490.
27. Anas, S. M., Shariq, M., & Alam, M. (2022). Performance of axially loaded square RC columns with single/double confinement layer (s) and strengthened with C-FRP wrapping under close-in blast. Materials Today: Proceedings, 58, 1128-1141.
28. Ahmadi, E., Alam, M., & Anas, S. M. (2022). Behavior of C-FRP laminate strengthened masonry and unreinforced masonry compound walls under blast loading, Afghanistan scenario. International Journal of Masonry Research and Innovation. DOI: 10.1504/IJMRI.2022.10049968
29. Anas, S. M., Alam, M., & Tahzeeb, R. (2022). Impact response prediction of square RC slab of normal strength

concrete strengthened with (1) laminates of (i) mild-steel and (ii) C-FRP, and (2) strips of C-FRP under falling-weight load. Materials Today: Proceedings. DOI: 10.1016/j.matpr.2022.07.324

30. Anas, S. M., Alam, M., Umair, M., & Kanaan, M. H. G. (2022). Strengthening of unreinforced braced masonry wall with (1) CFRP laminate and (2) mild-steel strips: innovative techniques, against close-range explosion. International Journal of Masonry Research and Innovation. DOI: 10.1504/IJMRI.2022.10051230
31. Anas, S. M., & Alam M (2022) Performance of brick-filled reinforced concrete composite wall strengthened with C-FRP laminate(s) under blast loading. Materials Today: Proceedings, 65, 1-11.
32. Anas, S. M., Alam, M., & Umair, M. (2022). Strengthening of braced unreinforced brick masonry wall with (i) C-FRP wrapping, and (ii) steel angle-strip system under blast loading. Materials Today: Proceedings, 58, 1181-1198.
33. Pellegrino, C., & Modena, C. (2006). Fiber-reinforced polymer shear strengthening of reinforced concrete beams: Experimental study and analytical modeling. ACI Structural Journal, 103(5), 720.
34. Cao, S., Zhis, W. U., & Wang, X. (2009). Tensile properties of CFRP and hybrid FRP composites at elevated temperatures. Journal of Composite Materials, 43(4), 315-330.
35. Dai, J. G., Gao, W. Y., & Teng, J. G. (2013). Bond-slip model for FRP laminates externally bonded to concrete at elevated temperature. Journal of Composites for Construction, 17(2), 217-228.
36. Wang, Z., Dai, J. G., Wang, M., Chen, L., Zhang, F., & Xu, Q. (2021). Residual bond strengths of epoxy and cement-bonded CFRP reinforcements to concrete interfaces after elevated temperature exposure. Fire Safety Journal, 103393.
37. Gao, W. Y., Dai, J. G., & Teng, J. G. (2015). Simple method for predicting temperatures in insulated, FRP-strengthened RC members exposed to a standard fire. Journal of Composites for Construction, 19(6), 04015013.
38. Gao, W. Y., Dai, J. G., & Teng, J. G. (2016). Fire resistance design of un-protected FRP-strengthened RC beams. Materials and Structures, 49(12), 5357-5371.
39. Gao, W. Y., Teng, J. G., & Dai, J. G. (2012). Effect of temperature variation on the full-range behavior of FRP-to-concrete bonded joints. Journal of Composites for Construction, 16(6), 671-683.
40. Zhao, J., Cai, G., Cui, L., Si Larbi, A., & Daniel Tsavdaridis, K. (2017). Deterioration of basic properties of the materials in FRP-strengthening RC structures under ultraviolet exposure. Polymers, 9(9), 402.
41. Dai, J. G., Yokota, H., Iwanami, M., & Kato, E. (2010). Experimental investigation of the influence of moisture on the bond behavior of FRP to concrete interfaces. Journal of Composites for Construction, 14(6), 834-844.
42. Zhang, F., Dai, J. G., Wang, Z., Wang, M., Leng, Y., & Xu, Q. (2021). Bond durability of epoxy and cement-bonded CFRP reinforcement to concrete interfaces subject to water immersion. Materials and Structures, 54(2), 1-12.
43. Dai, J. G., Yokota, H., Iwanami, M., & Kato, E. (2010). Experimental investigation of the influence of moisture on the bond behavior of FRP to concrete interfaces. Journal of Composites for Construction, 14(6), 834-844.
44. D’Antino, T., Focacci, F., Sneed, L. H., & Pellegrino, C. (2020). Shear strength model for RC beams with U-wrapped FRCM composites. Journal of Composites for Construction, 24(1), 04019057.
45. Calabrese, A. S., D'Antino, T., Colombi, P., & Poggi, C. (2020). Study of the influence of interface normal stresses on the bond behavior of FRCM composites using direct shear and modified beam tests. Construction and Building Materials, 262, 120029.
46. D’Antino, T., Carloni, C., Sneed, L. H., & Pellegrino, C. (2014). Matrix–fiber bond behavior in PBO FRCM composites: A fracture mechanics approach. Engineering Fracture Mechanics, 117, 94-111.
47. Triantafillou, T. C., & Papanicolaou, C. G. (2006). Shear strengthening of reinforced concrete members with

textile reinforced mortar (TRM) jackets. Materials and structures, 39(1), 93-103.

48. Al-Salloum, Y. A., Elsanadedy, H. M., Alsayed, S. H., & Iqbal, R. A. (2012). Experimental and numerical study for the shear strengthening of reinforced concrete beams using textile-reinforced mortar. Journal of Composites for Construction, 16(1), 74-90.
49. Escrig, C., Gil, L., Bernat-Maso, E., & Puigvert, F. (2015). Experimental and analytical study of reinforced concrete beams shear strengthened with different types of textile-reinforced mortar. Construction and building materials, 83, 248-260.
50. Contamine, R., Larbi, A. S., & Hamelin, P. (2013). Identifying the contributing mechanisms of textile reinforced concrete (TRC) in the case of shear repairing damaged and reinforced concrete beams. Engineering Structures, 46, 447-458.
51. Hou, W., Li, Z. Q., Gao, W. Y., Zheng, P. D., & Guo, Z. X. (2020). Flexural behavior of RC beams strengthened with BFRP bars-reinforced ECC matrix. Composite Structures, 241, 112092.
52. Awani, O., El-Maaddawy, T., and Ismail, N. (2017). Fabric-reinforced cementitious matrix: A promising strengthening technique for concrete structures. Construction and Building Materials, 132, 94-111.
53. Ombres, L. (2015). Structural performances of reinforced concrete beams strengthened in shear with a cement based fiber composite material. Composite Structures, 122, 316-329.
54. Schleser, M., Walk-Lauffer, B., Raupach, M., & Dilthey, U. (2006). Application of polymers to textile-reinforced concrete. Journal of Materials in Civil Engineering, 18(5), 670-676.
55. Koutas, L. N., Tetta, Z., Bournas, D. A., & Triantafillou, T. C. (2019). Strengthening of concrete structures with textile reinforced mortars: state-of-the-art review. Journal of Composites for Construction, 23(1), 03118001.
56. Huang, B. T., Wu, J. Q., Yu, J., Dai, J. G., Leung, C. K., & Li, V. C. (2021). Seawater sea-sand engineered/strain-hardening cementitious composites (ECC/SHCC): Assessment and modeling of crack characteristics. Cement and Concrete Research, 140, 106292.
57. Huang, B. T., Weng, K. F., Zhu, J. X., Xiang, Y., Dai, J. G., & Li, V. C. (2021). Engineered/strain-hardening cementitious composites (ECC/SHCC) with an ultra-high compressive strength over 210 MPa. Composites Communications, 26, 100775.
58. Xu, L. Y., Huang, B. T., & Dai, J. G. (2021). Development of engineered cementitious composites (ECC) using artificial fine aggregates. Construction and Building Materials, 305, 124742.
59. Zhu, J. X., Xu, L. Y., Huang, B. T., Weng, K. F., & Dai, J. G. (2022). Recent developments in Engineered/Strain-Hardening Cementitious Composites (ECC/SHCC) with high and ultra-high strength. Construction and Building Materials, 342, 127956.
60. Xu, L. Y., Huang, B. T., Lao, J. C., & Dai, J. G. (2022). Tailoring strain-hardening behavior of high-strength Engineered Cementitious Composites (ECC) using hybrid silica sand and artificial geopolymer aggregates. Materials & Design, 220, 110876.
61. Xu, L. Y., Huang, B. T., Lan-Ping, Q., & Dai, J. G. (2022). Enhancing long-term tensile performance of Engineered Cementitious Composites (ECC) using sustainable artificial geopolymer aggregates. Cement and Concrete Composites, 133, 104676.
62. Huang, B. T., Zhu, J. X., Weng, K. F., Li, V. C., & Dai, J. G. (2022). Ultra-high-strength engineered/strain-hardening cementitious composites (ECC/SHCC): Material design and effect of fiber hybridization. Cement and Concrete Composites, 129, 104464.
63. Ombres, L. (2012). Debonding analysis of reinforced concrete beams strengthened with fibre reinforced cementitious mortar. Engineering Fracture Mechanics, 81, 94-109.

64. Balaguru, P., Kurtz, S., & Rudolph, J. (1997). Geopolymer for repair and rehabilitation of reinforced concrete beams. Geopolymer Institute, St Quentin, France.
65. Dai, J. G., Munir, S., & Ding, Z. (2014). Comparative study of different cement-based inorganic pastes towards the development of FRIP strengthening technology. Journal of Composites for Construction, 18(3), A4013011.
66. Zhang, H. Y., Yan, J., Kodur, V., & Cao, L. (2019). Mechanical behavior of concrete beams shear strengthened with textile reinforced geopolymer mortar. Engineering Structures, 196, 109348.
67. Gao, W. Y., Hu, K. X., Dai, J. G., Dong, K., Yu, K. Q., and Fang, L. J. (2018). Repair of fire-damaged RC slabs with basalt fabric-reinforced shotcrete. Construction and Building Materials, 185, 79-92.
68. Duxson, P., Fernández-Jiménez, A., Provis, J. L., Lukey, G. C., Palomo, A., & van Deventer, J. S. (2007). Geopolymer technology: the current state of the art. Journal of Materials Science, 42(9), 2917-2933.
69. Marvila, M. T., de Azevedo, A. R. G., de Oliveira, L. B., de Castro Xavier, G., & Vieira, C. M. F. (2021). Mechanical, physical and durability properties of activated alkali cement based on blast furnace slag as a function of %Na2O. Case Studies in Construction Materials, 15, e00723.
70. Amran, M., Al-Fakih, A., Chu, S. H., Fediuk, R., Haruna, S., Azevedo, A., & Vatin, N. (2021). Long-term durability properties of geopolymer concrete: An in-depth review. Case Studies in Construction Materials, 15, e00661.
71. Xu, L. Y., Qian, L. P., Huang, B. T., & Dai, J. G. (2021). Development of artificial one-part geopolymer lightweight aggregates by crushing technique. Journal of Cleaner Production, 128200.
72. Turner, L. K., & Collins, F. G. (2013). Carbon dioxide equivalent (CO2-e) emissions: A comparison between geopolymer and OPC cement concrete. Construction and Building Materials, 43, 125-130.
73. Qian, L. P., Xu, L. Y., Huang, B. T., & Dai, J. G. (2022). Pelletization and properties of artificial lightweight geopolymer aggregates (GPA): One-part vs. two-part geopolymer techniques. Journal of Cleaner Production, 374, 133933.
74. Lao, J. C., Xu, L. Y., Huang, B. T., Dai, J. G., & Shah, S. P. (2022). Strain-hardening ultra-high-performance geopolymer concrete (UHPGC): Matrix design and effect of steel fibers. Composites Communications, 30, 101081.
75. de Azevedo, A. R., Cruz, A. S., Marvila, M. T., de Oliveira, L. B., Monteiro, S. N., Vieira, C. M. F., ... & Daironas, M. (2021). Natural fibers as an alternative to synthetic fibers in reinforcement of geopolymer matrices: a comparative review. Polymers, 13(15), 2493.
76. Li, W., Shumuye, E. D., Shiying, T., Wang, Z., & Zerfu, K. (2022). Eco-friendly fibre reinforced geopolymer concrete: A critical review on the microstructure and long-term durability properties. Case Studies in Construction Materials, e00894.
77. Zinkaah, O. H., Alridha, Z., & Alhawat, M. (2022). Numerical and theoretical analysis of FRP reinforced geopolymer concrete beams. Case Studies in Construction Materials, 16, e01052.
78. El-Sayed, T. A., & Algash, Y. A. (2021). Flexural behavior of ultra-high performance geopolymer RC beams reinforced with GFRP bars. Case Studies in Construction Materials, 15, e00604.
79. Peng, K. D., Huang, B. T., Xu, L. Y., Hu, R. L., & Dai, J. G. (2022). Flexural strengthening of reinforced concrete beams using geopolymer-bonded small-diameter CFRP bars. Engineering Structures, 256, 113992.
80. Wang, Y. S., Peng, K. D., Alrefaei, Y., & Dai, J. G. (2021). The bond between geopolymer repair mortars and OPC concrete substrate: Strength and microscopic interactions. Cement and Concrete Composites, 119, 103991.
81. Xu, L. Y., Huang, B. T., Li, V. C., & Dai, J. G. (2022). High-Strength High-Ductility Engineered/Strain-

Hardening Cementitious Composites (ECC/SHCC) Incorporating Geopolymer Fine Aggregates. Cement and Concrete Composites. 125, 104296.

82. Kong, D. L., & Sanjayan, J. G. (2010). Effect of elevated temperatures on geopolymer paste, mortar and concrete. Cement and Concrete Research, 40(2), 334-339.
83. Huang, J. Q., Xu, Y. Y., Huang, H., & Dai, J. G. (2022). Structural behavior of FRP connector enabled precast geopolymer concrete sandwich panels subjected to one-side fire exposure. Fire Safety Journal, 128, 103524.
84. Achillides, Z., & Pilakoutas, K. (2004). Bond behavior of fiber reinforced polymer bars under direct pullout conditions. Journal of Composites for construction, 8(2), 173-181.
85. Ahmad, F. S., Foret, G., & Le Roy, R. (2011). Bond between carbon fibre-reinforced polymer (CFRP) bars and ultra high performance fibre reinforced concrete (UHPFRC): Experimental study. Construction and Building Materials, 25(2), 479-485.
86. Peng, K. D., Zeng, J. J., Huang, B. T., Huang, J. Q., Zhuge, Y., & Dai, J. G. (2022). Bond performance of FRP bars in plain and fiber-reinforced geopolymer under pull-out loading. Journal of Building Engineering, 57, 104893.
87. ASTM C109 / C109M-20b, Standard Test Method for Compressive Strength of Hydraulic Cement Mortars (Using 2-in. or [50 mm] Cube Specimens), ASTM International, West Conshohocken, PA, 2020.
88. ASTM C39 / C39M-14, Standard Test Method for Compressive Strength of Cylindrical Concrete Specimens, ASTM International, West Conshohocken, PA, 2014.
89. ASTM D7205 / D7205M-06, Standard Test Method for Tensile Properties of Fiber Reinforced Polymer Matrix Composite Bars, ASTM International, West Conshohocken, PA, 2016.
90. ASTM A370-20, Standard Test Methods and Definitions for Mechanical Testing of Steel Products, ASTM International, West Conshohocken, PA, 2020.
91. Triantafillou, T. C. (1998). Shear strengthening of reinforced concrete beams using epoxy-bonded FRP composites. ACI Structural Journal, 95, 107-115.
92. Huang, B. T., Li, Q. H., Xu, S. L., & Li, C. F. (2017). Development of reinforced ultra-high toughness cementitious composite permanent formwork: experimental study and digital image correlation analysis. Composite Structures, 180, 892-903.
93. Huang, B. T., Zhu, J. X., Weng, K. F., Huang, J. Q., & Dai, J. G. (2022). Prefabricated UHPC-concrete-ECC underground utility tunnel reinforced by perforated steel plate: experimental and numerical investigations. Case Studies in Construction Materials, 16, e00856.
94. Li, Q. H., Yin, X., Huang, B. T., Luo, A. M., Lyu, Y., Sun, C. J., & Xu, S. L. (2021). Shear Interfacial Fracture of Strain-Hardening Fiber-Reinforced Cementitious Composites and Concrete: A Novel Approach. Engineering Fracture Mechanics, 107849.
95. ACI 318-19. Building code requirements for structural concrete. ACI Committee 318, Farmington Mills, MI; 2019, p. 622.
96. GB 50020-2010. Code for Design of Concrete Structures. Chinese Architecture Industry Press: Beijing; 2010 (in Chinese).
97. ACI 440.2R-08. Guide for the design and construction of externally bonded FRP systems for strengthening concrete structures. ACI Committee 440, American Concrete Institute. Farmington Mills, MI; 2008, p. 76.
98. ACI Committee 549. Guide to design and construction of externally bonded fabric reinforced cementitious matrix (FRCM) systems for concrete and masonry repair and strengthening. ACI 549.4R-13, Farmington Hills, MI, USA; 2013.

99. Escrig, C., Gil, L., Bernat-Maso, E., & Puigvert, F. (2015). Experimental and analytical study of reinforced concrete beams shear strengthened with different types of textile-reinforced mortar. Construction and building materials, 83, 248-260.
100. Zsutty, T. (1971). Shear strength prediction for separate catagories of simple beam tests. ACI Journal Proceedings, 68(2), 138-143.
101. ACI PRC-445-99 (2015) Recent Approaches to Shear Design of Structural Concrete (Reapproved 2015). American Concrete Institute, Farmington Hills, Michigan
102. Khuntia, M., Stojadinovic, B., & Goel, S. C. (1999). Shear strength of normal and high-strength fiber reinforced concrete beams without stirrups. ACI Structural Journal, 96(2), 282-289.